# Exploitation of Lanthanum as Stabilizing Agent in $NaFePO_4$ towards Electrochemical Performance in Sodium Ion Batteries

By

**KALAIYARASI V**

(Reg.No. 20PPH009)

Supervisor

**Dr.B.NALINI**

Department of Physics

A Thesis submitted to

Avinashilingam Institute for Home Science and Higher Education for Women,

Coimbatore-641 043

In Partial Fulfilment of the Requirements for the Degree of

**MASTER OF SCIENCE IN PHYSICS**

**MAY 2022**

# Exploitation of Lanthanum as Stabilizing Agent in $NaFePO_4$ towards Electrochemical Performance in Sodium Ion Batteries

By

**KALAIYARASI V**

(Reg.No. 20PPH009)

Supervisor

**Dr.B.NALINI**

Department of Physics

A Thesis submitted to

Avinashilingam Institute for Home Science and Higher Education for Women,

Coimbatore-641 043

In partial fulfilment of the requirements for the degree of

**MASTER OF SCIENCE IN PHYSICS**

**MAY 2022**

CERTIFIED AS A BONAFIED RESEARCH WORK

27/05/22

Signature of Head of the Department

27/05/2022

Signature of the Supervisor

# ACKNOWLEDGEMENT

I owe my sincere thanks to Lord Almighty and my parents for showering their generous blessings upon me in all endeavous.

I wish to express my gratitude to our chancellor, **Prof S.P.Thyagarajan,** Avinashilingam Institute for Home Science and Higher Education for Women, Coimbatore for providing all facilities to conduct this study.

I extend my thanks to **Dr. (Mrs) V.Bharathi Harishankar,** Ph.D., FRSA, Vice Chancellor, Avinashilingam Institute for Home Science and Higher Education for Women, Coimbatore for providing flamboyant help towards the completion of the study.

I record my deep sense of gratitude and indebtedness to **Dr. (Mrs) S.Kowsalya,** M.Sc.,M.Phil., Ph.D., Registrar, Avinashilingam Institute for Home Science and Higher Education for Women, Coimbatore for her help rendered throughout the course of this work.

I am also thanks to **Dr. (Mrs) G.Padmavathi,** M.Sc., M.Phil., Ph.D., Dean, School of Physical Sciences and Computational Sciences, Avinashilingam Institute for Home Science and Higher Education for Women, Coimbatore for granting the facilities required.

I whole heartedly thanks to **Dr. (Mrs)J.Shanthi**, M.Sc., M.Phil., Ph.D., Professor and Head of the Department of Physics, Avinashilingam Institute for Home Science and Higher Education for Women, Coimbatore for her encouragement and generous help which was of great value.

I am also thanks to Dr. **(Mrs.) N. S. Rajeswari,** M.Sc., M.Phil., M.C.A., SLET, Ph.D., Assistant Professor-SG and former Head of the Department of Physics, Avinashilingam Institute for Home Science and Higher Education for Women, Coimbatore for her help and support.

I express my heartiest thanks to my guide **Dr. (Mrs)B.Nalini**, M.Sc., Ph.D., M.S(Edu.Mgt), STA fellow, AIST Fellow (Japan), Assistant Professor, Department of Physics, Avinashilingam Institute for Home Science and Higher Education for Women, Coimbatore for her inspiring

guidance, meticulous care, patience, help, encouragement and motivation.

I express my gratitude to **(Mrs)P.Priyanka** and **(Mrs)G.G.Soundarya**, Research Scholar, Department of Physics, Avinashilingam Institute for Home Science and Higher Education for Women, Coimbatore for their valuable help in completion of my project.

I wish to express my special thanks to my parents, my friends and all my well-wishers for their constant encouragement, support and help in carrying out this work.

**V.KALAIYARASI**

**(20PPH009)**

## DECLARATION

I hereby declare that the project work entitled "**Exploitation of Lanthanum as Stabilizing Agent in $NaFePO_4$ towards Electrochemical Performance in Sodium Ion Batteries**" submitted to the Department of Physics, Avinashilingam Institute for Home Science and Higher Education for Women, Coimbatore, is a record of an original work done by me under the guidance of **Dr. (Mrs)B.Nalini,** Assistant Professor, Department of Physics and the project work is submitted in the fulfilment of the requirements for the degree of Master of Science in Physics. The results embodied in this have not been submitted to any other university or institute for the award of any degree or diploma.

V. Kal

**KALAIYARASI V**

**(20PPH009)**

**List of contents**

## List of Tables



## List of Figures

# CHAPTER I

# INTRODUCTION

Energy production and storage technologies have attracted a great deal of attention for day-to-day applications. Lithium-ion batteries (LIBs) are used in mobile electronic devices as well as in zero-emission electronic vehicles. Therefore, it remains unclear whether LIBs alone can satisfy the rising demand for small or mid-to-large-format energy storage applications. There are increasing concerns regarding load leveling of renewable energy sources and the smart grid as well as the sustainability of lithium sources due to their limited availability and consequent expected price increases. To mitigate these issues, research have been focused on alternative energy storage systems. Sodium-ion batteries (SIBs) are considered as the best candidate power sources because sodium is widely available and exhibits similar chemistry to that of LIBs. Sodiated layer transition metal oxides, phosphates and organic compounds have been introduced as cathode materials for SIBs. Some developments have been facilitated by the use of carbonaceous materials, transition metal oxides (or sulfides), intermetallic and organic compounds as anodes for SIBs. Apart from electrode materials, suitable electrolytes, additives, and binders were equally important for the development of practical SIBs. Hence sodium-ion batteries (SIBs) have been considered as a promising solution [1].

## 1.1 Electrochemical energy storage device

Energy storage plays a key role in storing the available resources of energy and utilizing them for future use. The common feature of this device is primarily to store the chemical energy through the electrochemical oxidation-reduction reverse process, and then this chemical energy is converted into electrical energy. Electrochemical energy storage devices include secondary batteries, flow batteries and supercapacitors. The electrochemical energy is related to fuel cells, photo electrochemical and energy storage systems such as batteries, super capacitors or ultra-capacitors [2].

## 1.2 Types of energy storage devices

### 1.2.1 Fuel cells

It is a galvanic cell that converts the chemical reaction energy of a continuously supplied fuel and an oxidizing agent into electrical energy.

A fuel cell is not an energy storage device but serves as a converter. The energy efficiency of a fuel cell is generally between 40% and 60%. If waste heat is captured in a cogeneration scheme, efficiencies of up to 85% can be reached.

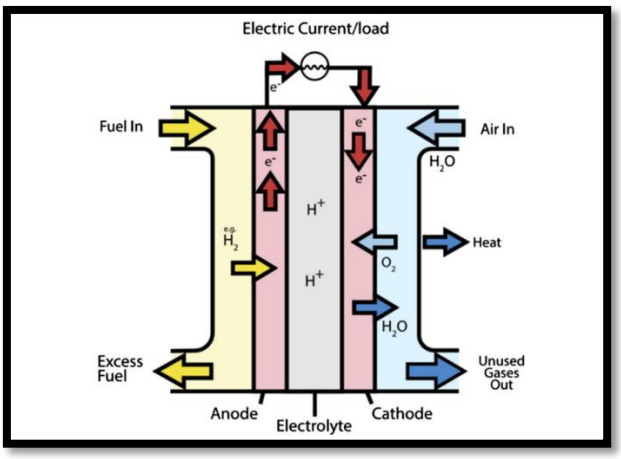


**Figure 1.1: Basic schematic diagram of a fuel cell**

A Fuel cell consists of two electrodes, one positive electrode called the anode, and one negative, called the cathode. These are separated by an electrolyte [3].

### 1.2.2 Photo electrochemical cell

Photoelectrochemical cells (PECs) extract electrical energy from light, including sunlight. It undergoes a process of artificial photosynthesis or electrolysis which converts chemical energy into electrical energy. Each cell consists of

- One or two semiconducting photoelectrodes
- Auxiliary metal and
- Reference electrodes immersed in an electrolyte.

PECs sustain over 19% solar-to-electrical conversion efficiency and electrolytic cells sustain over 18% solar conversion efficiency to hydrogen [4].

### 1.2.3 Supercapacitors

The supercapacitor has been matured significantly over the last decade and emerged with the potential to facilitate major advances in energy storage. Supercapacitors, also known as ultracapacitors or electrochemical capacitors, utilize high surface area electrode materials and thin electrolytic dielectrics to achieve capacitances several orders of magnitude larger than

conventional capacitors. Supercapacitors are able to attain greater energy densities still maintaining the characteristic high-power density of conventional capacitors.

Based upon current R&D trends, supercapacitors can be divided into three general classes:

- Electrochemical double-layer capacitors (EDLCs),
- Pseudo capacitors, and
- Hybrid capacitors.

In particular, supercapacitors have been great potential for applications that require a combination of high power, short charging time, high cycling stability, and long shelf life. There has been great interest in developing supercapacitors for electric vehicle hybrid power systems, pulse power applications, as well as back-up and emergency power supplies [5].

### 1.2.4 Batteries

Batteries are one of the dominant kinds of electrochemical energy storage. In a battery, electrical energy is stored as chemical energy. The chemical reactions occur throughout the bulk of the solid, and so the material must be designed to allow the access of the reacting species throughout the material and to allow its subsequent removal. This must occur thousands of times to provide a commercially viable rechargeable battery. All batteries are made up of three basic components: an anode, a cathode and some kind of electrolyte.

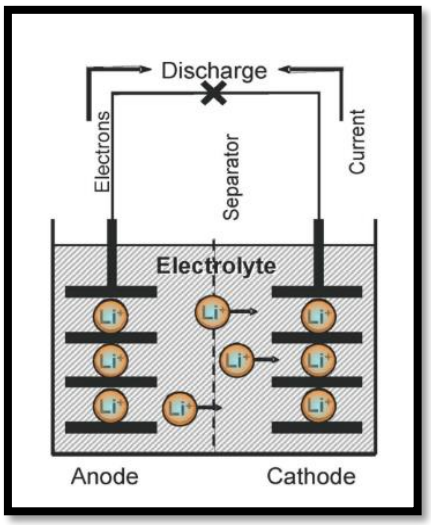


**Figure 1.2: Schematic diagram of a battery**

### 1.3 History of batteries

The first battery was Volta's cell (1800) that had alternating discs of zinc and copper separated by cardboard and using a brine solution as the electrolyte. The Volta cell evolved into the Daniel cell (1836) that had two electrolytes, and then into the Leclanche cell (1866) that used a zinc anode and a carbon anode. Rechargeable, also known as secondary, batteries have evolved over the years from lead acid (Gaston Plante in 1859) through nickel-cadmium (1899) and nickel-metal hydride, NiMH, (mid-1980s) to Li ion (1977). Ni-Cd batteries have been and are still extensively used in high-power consumer devices, such as gardening tools, electric razors, etc., and still are used as the starter batteries for aero engines [6].

### 1.4 Types of batteries

Batteries are basically classified into 2 types:

- Non-rechargeable batteries (primary batteries)
- Rechargeable batteries (secondary batteries)

#### 1.4.1 Primary batteries

A primary battery is a portable voltaic cell that is not rechargeable. These are batteries where the redox reactions proceed in only one direction. The reactants in these batteries are consumed after a certain period of time, rendering them dead. A primary battery cannot be used once the chemicals inside it are exhausted.

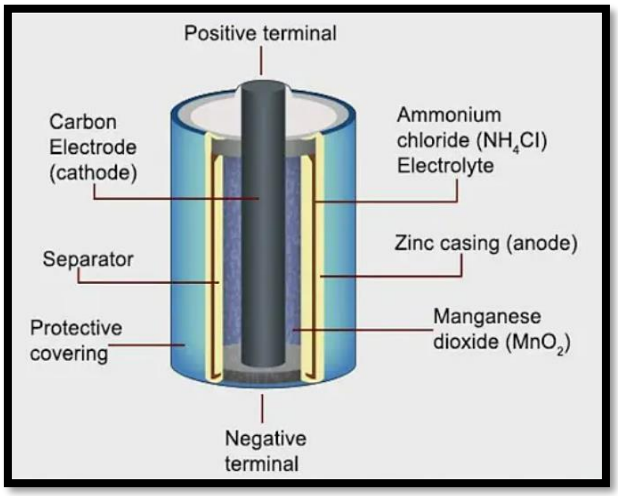


**Figure 1.3: Schematic diagram of Primary Battery**

An example of a primary battery is the dry cell. The household battery that commonly used to power TV remotes, clocks, and other devices. In such cells, a zinc container acts as the

anode and a carbon rod acts as the cathode. A powdered mixture of manganese dioxide and carbon is placed around the cathode. The space left in between the container and the rod are filled with a moist paste of ammonium chloride and zinc chloride. Another example of the primary cell is the mercury cell, where a zinc-mercury amalgam is used as an anode and carbon is used as a cathode. A paste of HgO is used as an electrolyte. These cells are used only in devices that require a relatively low supply of electric current (such as hearing aids and watches) [7].

There are mainly two types of primary cells.

- Alkaline Batteries
- Coin Cells

- **Alkaline Batteries**

In 1950s, alkaline batteries were created to overcome some of the performance concerns with zinc-carbon dry cells. They're made to be exact substitutes for zinc-carbon dry cells. Alkaline electrolytes, such as potassium hydroxide, are used in these batteries. A zinc-carbon dry cell of comparable size can offer three to five times the energy of an alkaline battery. Alkaline batteries are prone to leak potassium hydroxide, so they should be removed from devices before being stored for long periods.

- **Coin Cells Battery**

Coin cell batteries contain alkaline electrolytes as well as lithium and silver oxide compounds. These primary batteries are extremely effective at maintaining a constant and stable voltage.

### 1.4.2 Secondary Batteries

Secondary batteries are sometimes known as rechargeable batteries. These batteries can be utilized while also being recharged. They're usually made up of active ingredients that are released after use. Rechargeable batteries are recharged with electric current, which reverses the chemical reactions that occur during discharge. Chargers are electronic devices that supply the required current. Rechargeable batteries include those found in cell phones, MP3 players, and other electronic gadgets. Hearing aids and wristwatches generally need small batteries, as compared to phone exchanges and computer data centres which use larger batteries.

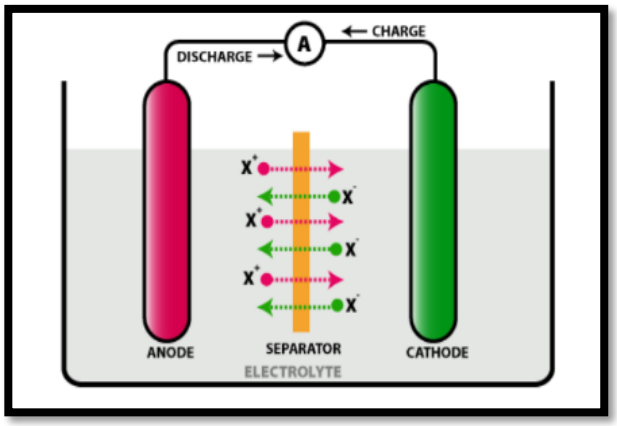


**Figure 1.4: Schematic diagram of Secondary Battery**

Types of Secondary Battery

- Lead - Acid Batteries
- Nickel - Cadmium Batteries
- Nickel - Metal Hydride Batteries
- Lithium - Ion Batteries

- **Lead – Acid Batteries**

By far the most popular and widely used rechargeable batteries are lead-acid batteries. Small, sealed cells with a capacity of 1 Ah to huge, sealed cells with a capacity of 12,000 Ah are all available in lead-acid batteries. Lead-acid batteries are widely employed in the automobile industry, where they are typically used as SLI Batteries (Starting, Lighting, and Ignition). Other uses for lead-acid batteries include,

- Energy storage
- Backup power
- Electric cars (including hybrids)
- Communication systems
- Emergency lighting

- **Nickel - Cadmium Batteries**

Along with lead-acid batteries, Nickel-Cadmium Batteries, or simply Ni-Cd Batteries, are some of the oldest batteries accessible today. They have a lengthy lifespan and are extremely dependable and durable. Ni-Cd batteries can withstand high discharge rates and function over a wide temperature range, which is one of its key advantages. Ni-Cd batteries

also have a very long shelf life. On a per Watt-hour basis, these batteries are more expensive than lead-acid batteries, but they are less expensive than other types of alkaline batteries.

- **Nickel -Metal Hydride Batteries**

These batteries are an advanced variant of nickel-hydrogen electrode batteries, which were previously only utilized in aerospace applications (satellites). Nickel Oxyhydroxide (NiOOH) serves as the positive electrode, while a metal alloy serves as the negative electrode, where hydrogen is stored reversibly. Nickel-metal hydride batteries have a higher specific energy and energy density than Ni-Cd batteries, which is one of their key advantages. Small cylindrical sealed nickel-metal hydride batteries are commercially available and are utilized in portable electronics.

- **Lithium-Ion Batteries**

The development of lithium-ion batteries has been amazing in the previous few decades. Lithium-ion batteries have been embraced by more than half of the consumer market. Laptops, mobile phones, cameras, and other electronic devices are among the most common uses for lithium-ion batteries [8].

### 1.5 Prevailing battery technologies

At the turn of the 20th century, more than one quarter of all cars in the United States were electric, yet the electric car had all but vanished by the 1920s. This disappearance was largely due to the insufficient range and power of electric car batteries compared to gasoline engines. Furthermore, electric cars were significantly more expensive than their gasoline counterparts. These same complaints are still heard today, even though battery technology has certainly improved over the last century. Much research and development are being done on battery technology to improve performance while ensuring that batteries are lightweight, compact, and affordable. Some of the new battery technologies are lithium-ion batteries, solid state batteries, aluminum-ion batteries, lithium-sulfur batteries and metal-air batteries [9].

### 1.6 Sodium-ion batteries

Sodium-ion batteries (NIBs) in particular are proving to be an emergent technology with potentially very attractive properties. They are potentially low cost and environmentally friendly with reduced supply risk. However, the development of NIBs faces various challenges

such as low gravimetric and volumetric energy densities and difficulty in achieving broader voltage windows. The use of Na can be extended to almost the whole spectrum of electrochemical energy storage systems. The new room temperature Na-S systems, high-energy Na-air technology, or high-power Na-based hybrid supercapacitors. In NIBs, most of the research efforts have been directed toward the improvement or finding of electrode active materials [10].

### 1.6.1 Basic concepts

For preparing a sodium-ion battery comprising a positive electrode and a negative electrode arranged to either side of an electrolyte, said positive electrode comprising, as the active material, a material made from sodium, said method comprising the following steps:

a) A step of depositing a sodium salt on the surface of the positive electrode, before placing same in the battery.

b) A step of assembling the positive electrode, the negative electrode and the electrolyte.

c) A step of forming a passivation layer on the surface of the negative electrode with the sodium ions from the decomposition of the sodium salt [11].

### 1.6.2 Cathode Materials for Na- ion Battery

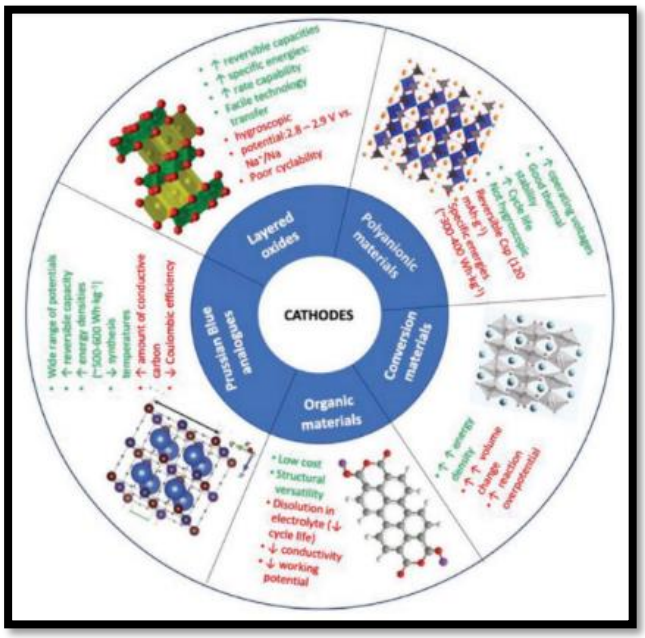


**Figure 1.5: Chemistry families explored as cathodes for Na-ion batteries with their strong and weak points (green and red, respectively).**

Similar to LIBs, highly reversible cathode materials based on the intercalation reaction, which involves interstitial introduction of a guest species ($Na^+$ in the present context), are needed for high capacity and good cyclability of SIBs. These electrode materials are mainly categorized into oxides, polyanions such as phosphates, pyrophosphates, fluorosulfates, oxychlorides, and NASICON (Na super ionic conductor) types, and organic compounds. These cathode materials exhibit a minimal structural change with intercalation, which ensures a reversible intercalation reaction that affects the cycle life.

Here, $NaFePO_4$ has been chosen as cathode material to enhance better electrochemical performance. It is best way to increase the ion mechanism and the addition of a trivalent dopant ($La^{3+}$) to $NaFePO_4$ since it is not available in earlier reports. However, continuous structural evolution is inevitable during $Na^+$ ion intercalation into the host structure interaction because of the large $Na^+$ ion size (coordination number 6: 1.02 Å) relative to that of $Li^+$. Also, sodiated transition metal materials are highly hygroscopic, even with brief exposure to air and caution is necessary to avoid hydration of the material, particularly the surface, which results in formation of NaOH that degrades electrode performance due to its insulating properties. Thus, the preparation of sodiated cathode materials and batteries requires meticulous handling and moisture-free conditions [1].

### 1.6.3 Anode material for Na-ion batteries

Negative electrode is a necessary part of Na-ion batteries. The optimization of Na-ion technology urgently needs improvement for the anode materials. It is desperately needed to seek for suitable anode materials with proper voltage window, high reversible capacity and stable structure. Research on anode materials for NIBs can be classified into five types:

- Carbon-based materials
- Alloy-based materials
- Metal oxides and sulfides based on conversion reaction
- Titanium-based composites with insertion mechanism
- Organic composites.

Most researches focus on the choice and synthesis of anode materials, few researches relate to the electrochemical Na-storage mechanism, which will pave the way for designing high performance anode materials. Therefore, more attention should be paid to the electrochemistry reaction mechanism [12].

### 1.6.4 Electrolytes for Na-ion batteries

The most common electrolyte formulations for sodium batteries use either $NaPF_6$ or $NaClO_4$ as salts in carbonate ester solvents, particularly propylene carbonate (PC). Unfortunately, metallic sodium anodes corrode continuously in the presence of most commonly used organic electrolytes, rather than forming a stable solid electrolyte interphase (SEI). There are many different methods for preparation of sodium ion conducting solid electrolytes. The most important methods are,

- Melt-quenching method
- Solution-cast method
- Hot-press technique
- Solid solution reaction technique [13].

### 1.6.5 Binder

Electrode binder is one of the important auxiliary functional materials in SIBs to enhance the contact, stabilize the electrode surface, and promote the dispersion of active materials and conductive agents. Although the binder has a small proportion in the battery, it has an important effect on the homogenizing process of the motor slurry, the maximum coating thickness and flexibility of the electrode, the energy density and cycle life of the battery.

Four commonly used binders, including

- Polyvinylidene fluoride (PVDF)
- Polyacrylic acid (PAA)
- Carboxymethyl cellulose (CMC)
- Styrene butadiene rubber (SBR) [14].

### 1.6.6 Comparison of the manufacturing costs for Li- ion batteries and Na-ion batteries

Sodium-ion batteries have been identified as appealing alternatives to lithium-ion batteries because they are made from raw materials that are less expensive, more abundant and less toxic. In the case of a shortage and associated price increase in lithium, the use of sodium can lead to substantial cost advantages. In the case of a shortage and associated price increase in lithium, the use of sodium can lead to substantial cost advantages. The advantage of SIBs is less dependent on the avoidance of lithium but rather of cobalt, the use of which is considered

inevitable in layered oxides for lithium-ion storage but is not required for sodium-ion storage. Further improvement may also be driven by aggravation of the identified raw material issues for LIBs, such as shortages in the supplies of lithium and cobalt, which would make lithium- and cobalt-free systems, such as SIBs, more attractive and cost-competitive alternatives [15].

### 1.6.7 Advantages of Na-ion batteries

- Na-ion batteries are low costs of raw materials
- Chemical reaction is free of corrosivity
- Long time charge will not cause battery damage, degradation, or self- discharge
- Long cycle life. At present the sodium-ion battery is at the technical verification stage [16].

## 1.7 Objective

To evaluate the electrochemical performance of $NaFe_{0.98}La_{0.02}PO_4$ compared to $NaFePO_4$ for sodium ion batteries.

- **Present day challenge**

Lithium-ion batteries (LIBs) are used in almost all the portable electronic devices. Since lithium is higher in cost and the less scarcity paves a way to go along with an alternate technology. Sodium ion batteries (SIBs) are promising candidate since sodium is highly abundant in earth's crust, low cost and exhibits similar chemistry as that of lithium.

- **Innovation statement**

Preparation of $NaFePO_4$ with metal ion doping could enhance the electrochemical properties. The novelty of the work is the addition of a trivalent dopant ($La^{3+}$) to $NaFePO_4$ since it is not available in earlier reports.

- **Approach**
  - To prepare $NaFePO_4$ and $NaFe_{0.98}La_{0.02}PO_4$ by sol-gel method.
  - To characterize the structural, morphological, and electrochemical studies.

# CHAPTER II

# REVIEW OF LITERATURE

A new mixed iron-based phosphate cathode material $Na_3Fe_2(PO_4)$ $(P_2O_7)$ have been synthesized using spray-drying method for SIBs by **Cao et al., (2020)** [17]. Reduced graphene oxide has been introduced to improve the electronic conductivity of the material. The modified cathode material $Na_3Fe_2(PO_4)$ $(P_2O_7)$ reduced graphene oxide composite exhibits a specific capacity of 110.2 $mAhg^{-1}$ at 0.1 C and a high-rate capability of 61.6 $mAhg^{-1}$ at 20 C. The electrochemical performance of the NFFPP and NFFPP@rGO cathode is investigated via a galvanostatic cycling test in a half-cell in a voltage window of 1.5-3.5 V (vs $Na^+$ /Na) using pure sodium metal as the anode. The NFFPP@rGO electrode maintains a reversible specific capacity of 93.6 $mAhg^{-1}$ while NFFPP maintains reversible specific capacity of only 35.6mAh $g^{-1}$ after 800 cycles at 1 C. Compared with the other iron-based phosphate cathodes such as $Na_3Fe_2(PO_4)_3$, $NaFePO_4$, $Na_2FeP_2O_7$, $Na_2FePO_4F$, etc., NFFPP@rGO exhibits an outstanding electrochemical performance, especially in terms of the theoretical specific capacity, cycle stability, and working potential.

The mixed phosphate $Na_4Fe_3(PO_4)_2P_2O_7$ have been implemented in thin film batteries for the first-time using solution combustion synthesis route by **Senthilkumar et al., (2020)** [18]**.** Galvanostatic charge/discharge analysis of the bulk $Na_4Fe_3(PO_4)_2P_2O_7$ sample was performed in Na-ion half-cell architecture in the voltage range of 1.8-3.8 V. The carbon-coated $Na_4Fe_3(PO_4)_2P_2O_7$ cathode delivered an initial discharge capacity of 126 $mAhg^{-1}$. When implemented in Na-ion half-cells, these thin films exhibited excellent electrochemical performance with robust cycling stability, similar to the bulk batteries. Almost, the $Na_4Fe_3(PO_4)_2P_2O_7$ thin films (∼220 nm) deliver reasonable electrochemical performance with good reversibility among all sodium insertion materials. The mixed phosphate $Na_4Fe_3(PO_4)_2P_2O_7$ forms an inexpensive and safe cathode for designing all-solid-state sodium-ion micro batteries.

Triphylite-$NaFePO_4$ have been successfully synthesized from Triphylite-$LiFePO_4$ by **Berlanga et al., (2020)** [19]**.** It can provide as a low-cost, eco-friendly method, enabling the recovery and subsequent reuse of lithium. The X-Ray diffraction patterns of the C/$LiFePO_4$, C/$FePO_4$ and C/$NaFePO_4$ were analysed. From XRD results, seen that the C/$FePO_4$ peaks are

shifted to a higher 2θ in comparison to the C/$LiFePO_4$ peaks and insertion of sodium ions into $FePO_4$ structure leads to larger unit cell parameters, and thus the peaks are shifted to lower 2θ. The FTIR analysis of the electrode material does not provide any extra information, the spectra only show the characteristic stretching and bending bands of $PO_4$ tetrahedra and no extra modes are observed. The electrochemical performance of C/$NaFePO_4$ was evaluated in Na-half cells in the voltage window 1.5-4 V. The capacity at the end of the first discharge was 132 $mAhg^{-1}$, which corresponds to ~86% of the theoretical capacity 154 $mAhg^{-1}$. The proposed synthesis route and electrochemical performance achieved makes C/$NaFePO_4$ a promising cathode material for future industrial applications in sodium-ion batteries.

A zero-strain cathode $Na_4Fe_7(PO_4)_6$ have been reported for the first time using facile spray drying method by **Pu et al., (2019)** [20]**.** It can also demonstrate negligible volume change (~0.24%) during $Na^+$ insertion/extraction as evidenced by ex situ X-ray diffraction. The NFP/C exhibits an excellent cycling stability with high Coulombic efficiency of nearly 100% in every cycle when used as a cathode material for room-temperature SIBs. The electrochemical behavior of NFP/C is quite similar to that of amorphous $NaFePO_4$ and $FePO_4$ in SIBs and the reversible capacity is 66.5 $mAhg^{-1}$ corresponding to 2.6 $Na^+$ insertion per formula unit. The cyclic voltammetry curves show a pair of prominent current peaks at 3.1 and 2.8 V in the anodic and cathodic processes. The NFP/C cathode tested at a low current density of 10 mA $g^{-1}$ also demonstrates excellent cycling performance without capacity decay in 120 cycles. This low-cost sodium ion phosphate can act as a promising cathode candidate for sodium ion batteries and is capable to boost the development of SIBs for grid-scale energy storage systems.

The iron-based phosphate composite ($Na_3Fe_2(PO_4)_3$@MCNT) have been synthesized using solid-state reaction method by **Xia et al., (2019)** [21]**.** When compared with the pure-phase $Na_3Fe_2(PO_4)_3$ the introduce tion of MCNT can effectively enhances the rate capability and cycle stability from 61 to 95 mAh $g^{-1}$ at 100 mAh $g^{-1}$ after 500 cycles. The CR 2016 coin-type cell was used to test the Electrochemical performances. At different scan rates include 0.02, 0.05, 0.1mV $s^{-1}$ in a voltage range of 1.5-3.5 V are implemented through Cyclic Voltammetry tests. The crystallinity of as-prepared powders is good and the lattice spacing of (131) crystal planes is 4.8 Å were indicated. The material exhibits excellent reversible specific capacity of 101 mA h $g^{-1}$ at 10 mA $g^{-1}$ and can reach high-rate capability up to 96 mA h $g^{-1}$ after 500 cycles at 100 mA $g^{-1}$. Due to its higher electronic conductivity and $Na^+$ diffusion

coefficient ($1.12\times10-10\ cm^2\ s^{-1}$) by introduction of MCNT to constitute a conductive network structure, it shows outstanding sodium-ion storage performance of $Na_3Fe_2(PO_4)_3$@MCNT electrode.

Defect chemistry, Na-ion diffusion paths and dopant properties in sodium iron phosphate $Na_3Fe_2(PO_4)_3$ cathode materials have been studied by **Kuganathan et al., (2019)** [22] which are employed through computational modelling techniques. $Na_3Fe_2(PO_4)_3$ shows a very high cyclic stability and reversible discharge capacity of $40mAhg^{-1}$ at about 2.5V. In computational methods, the General Utility Lattice Program (GULP) was used. Using the Broyden-Fletcher-Goldfarb-Shanno (BFGS) algorithm, the bulk $Na_3Fe_2(PO_4)_3$ and defect configurations were optimized. By doping with Zr on the Fe site and Si on the P site, the formation of Na vacancies and Na interstitials in this material can be facilitated. Doping with Zr on the Fe site can increase the concentration of Na vacancies while doping with Si on the P site can facilitate the formation of Na interstitials required for the improvement in the capacity of $Na_3Fe_2(PO_4)_3$.

A novel NASICON-type $K_{0.24}Na_{2.76}Fe2(PO_4)_3$ ($K_{0.24}$NFP) have been synthesized using simple solid-state reaction method by **Cao et al., (2019)** [23]. Ex-situ X-ray diffraction (XRD) were measured to identify crystal structures of the K-doped powders with the diffraction range 10-70°. The TG-DTA is concluded that the temperature was increased from 25 °C to 800 °C at a rate of 2 °C $min^{-1}$ under an air atmosphere. The scan rate of CV was 0.05, 0.08, 0.1, 0.2 and 0.5 mV $s^{-1}$ and potential window was 1.5-3.5 V. The charge/discharge curves, $K_{0.24}$NFP as cathode material in SIBs shows about 101.3 $mAhg^{-1}$, which is higher than all of other's K-doped materials and bare $Na_3Fe_2(PO_4)_3$. It still keeps a reversible specific discharge capacity of 73.6mAhg $^{-1}$ at 1000 mA $g^{-1}$. The sodium-ion storage capability of $K_{0.24}$NFP is prominently enhanced compared with bare-$Na_3Fe_2(PO_4)_3$. It is concluded that novel K-doped method improves the electrochemical performance of electrolyte materials for other energy storage devices like lithium-ion batteries or supercapacitors.

$AlF_3$-coated olivine $NaFePO_4$ have been obtained using facile electrochemical ion-exchange process in an aqueous electrolyte by **Jeong et al., (2019)** [24]. It is more environmentally friendly than conventional carbonate electrolytes. This electrochemical ion-exchange process is usually carried out as a two-step transformation from $LiFePO_4$ to $NaFePO_4$. In XRD analyses, crystalline structures of $FePO_4$ and $NaFePO_4$ obtained after the delithiation and sodiation processes were elucidated. The $AlF_3$-coating layer on $NaFePO_4$ is

approximately 10 nm as observed by TEM analysis. EDS analysis also confirmed the atomic ratios of $FePO_4$ (Na: Fe: P: O of 0: 1: 1: 4) and $NaFePO_4$ (Na: Fe: P: O of 1: 1: 1: 4). The olivine $NaFePO_4$ material displays a discharge capacity of 55.8 $mAhg^{-1}$ at 1 C with better surface stability in an aqueous electrolyte solution with the 0.5 wt% $AlF_3$ coating. A uniform elemental distribution of Na, P, Fe, O, Al, F, and C on the surfaces of $FePO_4$ are obtained for the pristine and $AlF_3$-coated $NaFePO_4$. The electrochemical performance shows that the discharge capacity is 95.6 $mAhg^{-1}$ at a 1 C rate and the capacity is 55.8 $mAhg^{-1}$ at 50 cycles. It is suggested that $AlF_3$ coatings are attractive for the surface stabilization of anode and cathode materials in aqueous rechargeable lithium- and sodium-ion batteries.

A new type of sodium iron phosphate ($Na_{0.71}Fe_{1.07}PO_4$) have been reported by **Zhu et al., (2018)** [25] which exhibits an extremely small volume change (~1%) during desodiation. The molar ratio of Na:Fe:P was investigated using ICP-AES, and found to be 0.71:1.07:1.00. The XRD pattern of NFP confirms the formation of a crystallized phase and indexed to an orthorhombic cell. The FTIR spectrum of the as-prepared NFP was dominated by the fundamental vibrations of $PO_4^{3-}$ , ruling out the existence of other polyanions such as $P_2O_7^{4-}$ and $P_3O_{10}^{5-}$ . When applied as a cathode material for SIBs, this new phosphate delivers a capacity of 78 $mAhg^{-1}$ even at a high rate of 50 C and maintains its capacity over 5,000 cycles at 20 C. The CV curves of the first five cycles at a scan rate of 0.1 $mVs^{-1}$ over a potential window of 1.5-4.3 V vs. $Na^+$ /Na. As a result of its superior electrochemical performance and the elemental abundance, the new material is believed to be promising for future large scale rechargeable batteries.

$NaFePO_4$@C nanofibers have been prepared using electrospinning technique by **Liu et al., (2018)** [26]. The ultrasmall nano size effect as well as a high-potential desodiation process can transform the generally perceived electrochemically inactive maricite $NaFePO_4$ into a highly active amorphous phase. The electrochemical performance in terms of high reversible capacity 145 $mAhg^{-1}$ at 0.2 C, high-rate capability 61 $mAhg^{-1}$ at 50 C and high cyclic stability ≈89% capacity retention over 6300 cycles is achieved. CV curves with voltage ranging from 1.5 to 4.5 V at different scan rates 0.1-2.0 mV $s^{-1}$. Such fascinating overall performance has scarcely been reported for the $NaFePO_4$ based SIB cathodes and also outstanding among all the Na-storage cathodes reported. It can effectively improve the active materials utilization rate, facilitate the electrons/$Na^+$ ions transport and strengthen the electrode stability cycling that leading to the fascinating Na-storage performance.

Nanosized maricite-type phase of sodium iron phosphate (m-NFP) have been proposed into two entirely different approaches and its composite with carbon using novel DMSO-assisted, Pechini approaches and solid-state method by **Kapaev et al., (2017)** [27]. Electrochemical tests were carried out using a ZRU 50 mA 10 V charge-discharge system in a voltage range of 1.5-4.1 V vs. $Na/Na^+$ at a current density of 15 $mAg^{-1}$. The Raman spectra of NFP-PE@C and NFP-DMSO@C samples had two bands at 1600 and 1350 $cm^{-1}$. According to the high-resolution transmission electron microscopy (HRTEM) images, ball-milled NFP-PE@C consisted of agglomerated particles and interlayer distances of 0.26 and 0.37 nm, which correspond to [301] and [111] hkl lattice planes of m-NFP, respectively. The m-NFP capacity growth caused by the ball-milling can be explained mainly by the structural disordering in m-NFP and the formation of electrochemically active amorphous phases.

The effect of polythiophene (PTh) coating revealed the mechanism of $Na^+$ (de)intercalation from/in $NaFePO_4$ using ex situ XRD and in situ X-ray absorption spectroscopy have been studied by **Ali et al., (2016)** [28]. The fabrication of $NaFePO_4$, $FePO_4$/PTh was sodiated using an excess of NaI (NaI: $FePO_4$ ratio of 1.1:1) in acetonitrile under argon reflux. Fourier transformation of the EXAFS spectra was performed in the k-range from 2 to 13 Å-1, and the resulting spectra were fitted in the R-range from 1 to 4 Å with the $k^2$ weight. Olivine $NaFePO_4$ was prepared using sequential processes, including an ion-exchange reaction between $Li^+$ and $Na^+$ via chemical delithiation of $LiFePO_4$ and sodiation of $FePO_4$. To investigate the coating effect, uncoated and PTh-coated $NaFePO_4$ electrodes were galvanostatically cycled at a current density of 10 $mAg^{-1}$ in the potential range between 2.2 and 4.0 V. A high reversible capacity of 142 $mAhg^{-1}$ is obtained for a current density of 10 $mAg^{-1}$, and a high retention capacity of 93% over 100 cycles is observed with a round-trip efficiency greater than 99%. The advantages of $NaFePO_4$ include its low cost, high reversibility and long cycle life, which makes it suitable for SIBs as grid storage applications.

An electrochemical driven ion-exchange process have been investigated which transform olivine $LiFePO_4$ into highly pure olivine $NaFePO_4$ by **Tang et al., (2016)** [29]. This shows superior electrochemical performance and the olivine phase $NaFePO_4$ synthesized via organic-based electrochemical insertion of sodium ions into chemically or electrochemically delithiated $FePO_4$. The amorphous $NaFePO_4$ exhibited exceptional performance with ultrastable capacity up to 150$mAhg^{-1}$ in the potential range of 1.5-4V with a sloping charge/discharge plot. Using XRD and ICP to determine the phase purity of as-prepared samples. The aqueous ion exchanged $NaFePO_4$ exhibits high reversible capacity of 142 $mhg^{-1}$

(0.1C) as well as impressive cycle stability 6000 cycles at 10C. Such a good cycle stability should be attributed to the complete substitution of $Li^+$ by $Na^+$ in $NaFePO_4$, which ensures unrestricted one-dimensional (1D) channels for Na+ insertion/extraction. The results indicate that the relaxation of $Na_xFePO_4$ particles occurs during the solid-solution stage during desodiation, resulting in biphasic separation due to $NaFePO_4$ and $Na_{2/3}FePO_4$ upon equilibrium.

Nanostructured pure $Na_2FePO_4F$ have been synthesised using soft template method by **Law et al., (2015)** [30]. Powder X-ray diffraction was performed using Cu-Kα radiation operated at 40 kV and 30 mA from an angle 2θ of 10° to 60°. The samples were coated with a thin platinum layer to increase the surface conductivity observed by FESEM analysis. In TGA analysis, the experiment was performed in air at a heating rate of 5°C $min^{-1}$ starting from room temperature to 600°C. The High-Energy Ball Milling (HEBM) sample delivered a discharge capacity of 116 and 78mAh $g^{-1}$ at 0.1 C and 1 C respectively while pristine sample without the HEBM process demonstrated a relatively low sodium storage performance of 87mAhg $^{-1}$ at 0.1 C. Cyclic voltammetry (CV) experiment was carried out on coin-cells between 2.0-4.0 V, at a scan rate of 0.05 mV $s^{-1}$ at room temperature. The HEBM sample exhibited stable cycling performance up to 200 cycles at 1 C, retaining almost 80% of its initial capacity with an average coulombic efficiency of 99.4%. The improved sodium storage performance as compared to the pristine sample is discussed in terms of the reduced antisite disorder and associated sodium ion diffusion.

Hollow amorphous $NaFePO_4$ nanospheres have been fabricated using simple in situ hard template approach by **Li et al., (2015)** [31]. It can be seen that the as-prepared hollow $NaFePO_4$ nanospheres are poorly crystalline or amorphous because of absence of peaks in the XRD pattern. The high-resolution STEM image also suggests an amorphous nature because no discernible lattice fringes can be observed. The cyclic voltammogram curve shows a pair of current peaks positioned at 2.86 and 2.32 V corresponding to the de-intercalation/intercalation. The cycling stability of $NaFePO_4$ nanospheres is superior to those of other reported $NaFePO_4$ materials. After high-rate charge discharge cycling, a specific capacity of 147.8 $mAhg^{-1}$ is restored when the current density is decreased to 0.2C. The outstanding electrochemical performance of the as-prepared hollow amorphous $NaFePO_4$ nanospheres as cathode materials for SIBs. It also provides a large electrochemical reaction interface that drastically decreases the electrochemical polarization and improves the capacity utilization as well as rate capability of the electrode.

Pristine and carbon-coated $NaFePO_4$ and $Na_2FePO_4$ have been prepared using solid state synthesis by **Kosova et al., (2014)** [32]. The XRD patterns of as prepared $NaFePO_4$ and $Na_2FePO_4$ samples were recorded. In situ X-ray study performed by means of temperature-controlled X-ray chamber showed that intensity of $Na_2FePO_4$ increased and decreased depend upon temperature levels. The FTIR spectrum of the $NaFePO_4$ + NaF activated mixture though being less intensive and low-resolved. SEM and TEM analysis of $NaFePO_4$ samples shows fine particles growth (200 nm size). Charge- discharge capacity of 19mAh $g^{-1}$ was achieved in the 2.0-4.2 V voltage range. Carbon-coated $Na_2FePO_4F$ shows discharge capacity of 116 mAh $g^{-1}$ at 0.1 C rate within the 2.0-4.2V voltage range and a good cyclability. The $Na_2FePO_4$ reveals facile $Na^+/Li^+$ ion exchange both in electrochemical and chemical process up to $NaLiFePO_4F$ composition.

A new compound High Pressure-$Na_2Co$ [$PO_4$] F have been proposed using high-pressure solid-state reaction by **Yahia et al., (2014)** [33]**.** The crystal structure was determined from single crystal X-ray diffraction data. The calculated density of HP-$Na_2Co$ [$PO_4$] F is greater than the average density of α-$NaCoPO_4$ and NaF. Galvanometric cycling tests were performed in the potential range of 1.5-4.8 V or 1.5-5.0 V at a rate of C/50.This study reveals that under high temperature and pressure, the layered compound Atmosphere pressure [AP], (AP or HP)-$Na_2Co$ [$PO_4$] F is transformed to a 3D-framework. When the sample was charged to 5.0 V in Na-half-cell, a charge capacity of 125 $mAhg^{-1}$ was observed and while the sample was charged to 4.8 V in a Li-ion half-cell, a charge capacity of 80 $mAhg^{-1}$ was observed. The high-pressure forms of the $Na_2Mn$ [$PO_4$] F and $Na_2Fe$ [$PO_4$] F compounds have also been investigated.

Olivine $NaFePO_4$ have been studied which has the same phase structure as olivine $LiFePO_4$ by **Zhu et al., (2013)** [34]. Both thermodynamics and reaction kinetics for Na-ion insertion/extraction in $NaFePO_4$ are quite different from the lithiation/delithiation process in $LiFePO_4$. A systematic comparison between olivine $LiFePO_4$ in Li-ion batteries and $NaFePO_4$ in Na-ion batteries is critical for further improving the electrochemical performance of $NaFePO_4$ in Na-ion batteries. All C-rates used in calculated based on the theoretical capacity of 154 mA h $g^{-1}$ for $NaFePO_4$ and 170 mA h $g^{-1}$ for $LiFePO_4$. Cyclic voltammetry tests with voltages ranging from 2.0 V to 3.8 V for the $NaFePO_4$ cell and 2.5 V to 4.0 V for the $LiFePO_4$ cell were performed under various scan rates. Electrochemical performances of C-$NaFePO_4$ and C-$LiFePO_4$ are compared shows the cycling stability of the C-$NaFePO_4$ cell at a constant current of 0.1 C (15.4 mA $g^{-1}$). All C-rates are calculated based on the theoretical capacity of

$NaFePO_4$ (154 mA h $g^{-1}$). One potential plateau during Na-ion insertion and two potential plateaus for Na-ion extraction from $NaFePO_4$ and the two potential plateaus were corresponding to the formation of the intermediate $Na_{0.7}FePO_4$ phase during phase transition from $NaFePO_4$ to $FePO_4$ are reported.

Carbon coated porous hollow $Na_2FePO_4F$ ($C/Na_2FePO_4F$) spheres have been synthesized using ultrasonic spray pyrolysis process by **Langrock et al., (2012)** [35]. To determine the amount of carbon between 6 and 8 wt% were analysed from Energy dispersive X-ray spectroscopy and thermogravimetric analysis. $C/Na_2FePO_4F$ can deliver approximately 80 mAh $g^{-1}$ of reversible capacity at 0.1C and 26 mAh $g^{-1}$ at 9C while the sample synthesized using solid-state reaction can only provide 15 mAh $g^{-1}$ at the rate of 8C. The high-rate performance of $C/Na_2FePO_4F$ is attributed to high interface area between liquid electrolyte and $C/Na_2FePO_4F$ due to penetration of the liquid electrolyte into pores and centre hole of hollow $C/Na_2FePO_4F$ and carbon coating increasing the charge transfer reaction kinetics then hollow structure shortening the diffusion length of $Na^+$ ion. Furthermore, the presence of a thin carbon layer acts to enhance the rate capability and cycling stability. In electrochemical performance of hollow $C/Na_2FePO_4F$ spheres combined with mature aerosol spray synthesis technology make these carbon coated porous hollow $C/Na_2FePO_4F$ spheres very promising as cathode materials for practical applications in Na-ion batteries.

A new cathode compound $Na_2FeP_2O_7$ have been reported for sodium-ion batteries with promising electrochemical properties involving a 3.0 V $Fe^{3+}/Fe^{2+}$ redox activity using conventional one-step solid-state route by **Barpanda et al., (2012)** [36]. Galvanostatic charge-discharge cycling was conducted in the voltage range of 2.0-4.0 V at different rates (from C/20 to 10 C) (at 25 °C). The electrochemical performance of solution-combustion prepared $Na_2FeP_2O_7$ cathode with no further cathode optimization such as carbon coating or particle down-sizing. From SEM analysis, the particle size was estimated to be 3–5 μm for solid-state synthesis and 300-500 nm for solution-combustion synthesis. The electrochemical cycling at a rate of C/20 (at 25 °C), a reversible capacity of 82 $mAh \cdot g^{-1}$ was obtained approaching one-electron theoretical capacity of 97 $mAhg^{-1}$. With its convenient synthesis, low cost, theoretical capacity close to 100 $mAhg^{-1}$, excellent reversibility and rate capability, $Na_2FeP_2O_7$ is a promising cathode material for future sodium-based batteries.

Sodium iron phosphate ($NaFePO_4$) have been synthesized using Pechini method by **Sun et al., (2012)** [37]. The characterized material using $LiPF_6$ (Lithium hexafluoro phosphate) as the electrolyte salt in carbonate/diethyl carbonate solvents. Varying different temperature and environments (Ar, $N_2$,5% $H_2$/Ar etc..), the materials were synthesized and compared with each other. For electrochemical investigation, samples annealed in Ar atmosphere were used. Sodium is almost heavier with an atomic weight of 22.99g $mol^{-1}$ compared to 6.941g $mol^{-1}$ for that of lithium. The X-ray diffraction shows the formation of $Fe_2O_3$ and $Na_3Fe(PO_4)_3$. The charge and discharge curves for $NaFePO_4$ shows an increase in capacity with every cycle. The presence of lithium and sodium could be detected in electrode by XPS. Analyzing the impedance curves, both ohmic and diffusion-controlled resistance were decreased. Although the material shows very low capacity around 30mAh $g^{-1}$ the longer cycle life of these cells is promising. Further, these materials could be used for large scale energy storage systems and grid applications.

Lithium iron phosphate ($LiFePO_4$) have been efficiently converted to sodium iron phosphate ($NaFePO_4$) using electrochemical deposition process by **Oh et al., (2012)** [38]. It could be used as cathode in sodium ion battery. According to procedure, $LiFePO_4$ powder was prepared by co-precipitation method. The Na/$NaFePO_4$ cell was then galvanostatically cycled at various C-rates in the 2.0 V- 4.3 V voltage range. The voltage profile of this cell associated with the $FePO_4$-$NaFePO_4$ process is calculated to the order of 125 $mAhg^{-1}$ were reported. The sodiation process is analyzed by XRD revealed that the formation of the olivine $NaFePO_4$ has indeed been achieved by the electrochemical process. The electrochemical properties of $NaFePO_4$ electrodes are not affected by the increase in lattice parameters. The charge-discharge polarization observed is most likely due to the poor electronic and ionic conductivity of $FePO_4$ phase. Specific capacities varying from 125 $mAhg^{-1}$ to 85 $mAhg^{-1}$ with reasonably limited cell polarizations. The electrochemical method is very promising to achieve satisfactory battery performances and results suggest that the $NaFePO_4$ here studied can be proposed as a valid cathode material for rechargeable sodium battery.

Carbon-coated $Na_2FePO_4F$ have been synthesized using solid state method by **Kawabe et al., (2011)** [39]**.** It shows relatively high operating voltage Ca 3.0V vs Na and fair reversibility. Carbon coating is an effective way to improve electrode performance and reducing the particle size. They demonstrate the possibility of carbon coated $Na_2FePO_4$ as the positive electrode for rechargeable sodium ion batteries. Electrode performance of $Na_2FePO_4F$ for rechargeable sodium batteries is also examined. Coin type cells were assembled to evaluate

the electrode performance of $Na_2FePO_4F$. It delivers initial discharge capacity of 110 $mAhg^{-1}$ at a rate of 1/20C (6.2 $mAg^{-1}$) with well-desired voltage plateau at 3.06 and 2.91V vs Na metal. Also, concluded that carbon coated $Na_2FePO_4F$ is one of the good candidate electrode materials for rechargeable sodium batteries.

A layered iron (III) phosphate phase $Na_3Fe_3(PO_4)_4$ have been synthesized using solid-state reaction method by **Trad et al., (2010)** [40]. All the diffraction peaks of the XRD pattern were indexed using the monoclinic C2/c space group. The XRD and Mossbauer spectroscopy confirmed that there is no chemical reaction with the electrolyte used. The galvanostatic cycling and OCV curves obtained for $Na_3Fe_3(PO_4)_4$ prepared by solid-state reaction method was used as a positive electrode in lithium cell. Up to 1.9 $Li^+$ ions/f.u could be intercalated and only 1.7 $Li^+$ ions could be extracted between 2 and 4.5 V vs $Li^+$ /Li with an average voltage of around ~2.8 V. The cycling curve obtained with $Na_3Fe_3(PO_4)_4$ used as a positive electrode in a sodium cell and it exhibits a low polarization of around 0.03 V for a C/100 cycling rate, indicating rather good ionic and electronic conductivities of the electrode. To improve its electrochemical performances, $Na_3Fe_3(PO_4)_4$ was also prepared via a hydrothermal method that leads to a significant particle size reduction. Therefore, no clear improvements in the cycling performances were observed using this material as the positive electrode in sodium and lithium batteries.

**Table.2.1: Review table on Sodium iron phosphate and its electrochemical performance**

| **Author [Year Of Publication]** | **Material Used** | **Method of Preparation** | **Electrochemical Performance** |
|---|---|---|---|
| **Rahmawati et al., (2021)** [41] | $NaFePO_4$, $FePO_4$/Al (NFP(A)), $LiFePO_4$/Al (NFP(B)) | Solid-state reaction | • CV- voltage range from 2.0-4.0 V using a scan rate of 0.05 $mVs^{-1.}$<br>• By reducing the scan rate to as low as 0.04 $mVs^{-1}$, electrical conductivity increased for both NFP(A) and NFP (B). |

| | | | |
|---|---|---|---|
| **Bong et al., (2021)** [42] | Amorphous $NaFePO_4$ | Simulated melt-quenching | • It is able to deliver a first cycle capacity of 142 $mAhg^{-1}$ and retains 95% of its capacity over 200 cycles. |
| **Rahmawati et al., (2020)** [43] | $NaFePO_4$ | Caustic fusion method | • CV- voltage range 2.0 -4.0 V with 0.05 $mVs^{-1}$ of the scan rate.<br>• The olivine structure shows better performance than maricite providing 154 $mAhg^{-1}$.<br>• Impedance analysis found that the prepared-$NaFePO_4$ provide 1735Ω resistance or comparable to 5.36 x $10^{-6}$ $Scm^{-1}$. |
| **Hilder et al., (2018)** [44] | Sodium iron phosphate (NFP) | Chemical delithiation/ sodiation method | • Excellent cycling performance with a capacity of 85 $mAhg^{-1}$ and a capacity retention of 95% over 100 cycles |
| **Chen et al., (2017)** [45] | Carbon-coated $Na_2FeP_2O_7$ | Facile urea-nitrate combustion method | • It can deliver a stable reversible capacity of 78 mAh $g^{-1}$ at 1 C for 300 cycles<br>• Retains a reversible capacity of 18 mAh $g^{-1}$ for 20 cycles even at a current density reaching up to 50 C. |
| **Zhao et al., (2017)** [46] | Carbon-coated $NaFePO_4$ ($NaFePO_4$/C) | Two-step solid state method | • The initial reversible capacity of 48.8 mAh $g^{-1}$ at 0.05 C<br>• The reversible capacity of 50.6 and 38 mAh $g^{-1}$ can be obtained at 0.1 C, 0.2 C. |

| | | | |
|---|---|---|---|
| **Yao et al., (2017)** [47] | $Na_2Fe(C_2O_4)F_2$ | Hydrothermal synthesis | • It has capable of reversibly inserting 0.56 $Na^+$ per unit formula unit up to 50 cycles |
| **Yang et al., (2016)** [48] | Maricite structure $NaFePO_4$ | Electrospinning method | • Initial charge-discharge curve and rate capability of $Na_{0.9}FePO_4$ at 1.5- 4.5 V.<br>• The rate capability retention was increased to a 0.05 C-rate, after cycling resulting in retention of 110-130% compared to before the first cycle |
| **Kim et al., (2014)** [49] | Maricite $NaFePO_4$ powder | Solid-state method | • It delivered a capacity of 142 $mAhg^{-1}$ (92% of the theoretical value) at the first cycle.<br>• It showed outstanding cyclability with a negligible capacity fade after 200 cycles (95% retention of the initial cycle) |
| **Wongittharom et al., (2013)** [50] | Na/$NaFePO_4$ with an Olivine crystal structure | Electrochemical sodiation method | • The charge-discharge performance of the Na/$NaFePO_4$ cells with in a cell voltage range of 2.0-3.8 V)<br>• The maximum discharge capacity (at 0.05 C) of $NaFePO_4$ was 120 mAh $g^{-1}$.<br>• $NaFePO_4$ capacity of 125 $mAhg^{-1}$ (at 0.05 C) was obtained in the 0.5 M NaTFSI-incorporated IL. |
| | | | • CV voltage range from 2.3-3.0 V |

| | | | |
|---|---|---|---|
| **Chihara et al., (2013)** [51] | $Na_3M_2(PO_4)_2F_3$ [M = Ti, Fe, V] | Two-step solid-state synthesis | • It exhibited stability on cycling and a capacity of approximately 120 $mAhg^{-1}$.<br>• The measured first discharge capacity was 119.8 $mAhg^{-1}$ and the stable cyclability of the cathode at approximately 110 mAh $g^{-1}$. |
| **Zhu et al., (2012)** [52] | Carbon-coated olivine $NaFePO_4$ ($C\text{-}NaFePO_4$) | Chemical delithiation and subsequent electrochemical sodiation method | • CV voltage range from 2.0 V to 3.8 V for $NaFePO_4$ cells.<br>• The cycling stability of the $C\text{-}NaFePO_4$ cell at a constant current of 0.1 C (15.4 $mAg^{-1}$).<br>• It can deliver approximately a reversible capacity of 100 $mAhg^{-1}$. |
| **Zaghib et al., (2011)** [53] | $NaFePO_4$ | Hydrothermal route | • The cells were galvanostatically cycled between 1.7V and 4.0V vs. $Na^0/Na^+$.<br>• Discharge–charge curves of a $Na/NaPF_6$ in EC–DEC/$FePO_4$ cell at C/24 rate in the potential window 3.0-1.5V.<br>• The discharge capacity of 147 mAh $g^{-1}$ could be obtained for NaFePO4 in the olivine phase, and full insertion of Na can be achieved at 1.7V. |

# CHAPTER III

# MATERIALS AND METHODS

## 3.1 INTRODUCTION

This chapter deals with the experimental techniques used in the preparation and characterization of Sodium iron phosphate ($NaFePO_4$) and La doped $NaFePO_4$ ($NaFe_{0.98}La_{0.02}PO_4$). The method adopted for the synthesis of the chosen material is sol-gel technique. The properties of the material are analyzed by employing some of the experimental techniques such as,

- X-ray Diffraction (XRD)
- Field Emission Scanning Electron Microscope (FESEM)
- Thermogravimetric-Differential thermal analysis (TG-DTA)
- Raman Spectroscopy (RS)
- Cyclic Voltammetry (CV)

## 3.2 Preparation of $NaFePO_4$ and $NaFe_{0.98}La_{0.02}PO_4$

$NaFe_{0.98}La_{0.02}PO_4$ was synthesized via the sol-gel method. Initially, appropriate amounts of ferrous oxalate dihydrate and sodium nitrate are dissolved in 60 ml solution of diluted nitric acid [Sol A]. Sol A is stirred until the salts get completely dissolved. 10 ml of Ammonium dihydrogen phosphate [Sol B] is stirred until it gets dissolved in water. A 20 ml of citric acid [Sol C] is dissolved in distilled water under magnetic stirring. Sol B and C were added to sol A and it is kept at 150°C under magnetic stirring until a gel is formed. The obtained gel is kept in water bath at 150°C for 3 hours and a dry product is obtained after the removal of excess ammonia from the sample. And it is finely ground and calcined at 700°C for 2 hours. The same procedure is repeated for the La doped sample by the addition of 0.02g of Lanthanum (III) nitrate hexahydrate along with Sol A. These samples are taken for further characterizations.

### 3.2.1 Electrochemical testing:

Electrochemical studies are carried out using $NaFePO_4$ and $NaFe_{0.98}La_{0.02}PO_4$ as working electrode, and it is composed of a mixture of active material, polyvinyl fluoride (PVDF) as binder and carbon black as conductive in the ratio of 85:10:5. Then the mixture is mixed with N-methyl pyrrolidinone (NMP) solvent to form a slurry. Then the slurry is coated on copper foil, and dried at 80°C to ensure the complete evaporation of NMP. The prepared

electrode is tested in alkaline electrolyte viz., 1M sodium hydroxide (NaOH) pellets which is dissolved in distilled water. The prepared electrode is tested using three electrode system with $NaFePO_4$ and $NaFe_{0.98}La_{0.02}PO_4$ as the working electrode, Ag/AgCl as the reference electrode and platinum as the counter electrode.

### 3.3. CHARACTERIZATION TECHNIQUES:

This chapter describes the principle, working and experimental set ups utilized for various measurements towards the characterization of the synthesized sodium iron phosphate. The techniques adopted to characterize the nanoparticles are: X - ray diffraction (XRD), Field Emission Scanning Electron Microscopy (SEM), Raman Spectroscopy (RS), Thermogravimetric-Differential thermal analysis (TG-DTA) and Cyclic voltammetry (CV).

### 3.3.1 POWDER X-RAY DIFFRACTION (XRD)

X-ray diffraction (XRD) is a powerful non-destructive technique for characterizing crystalline materials. It provides information on structures, phases, preferred crystal orientations (texture), and other structural parameters, such as average grain size, crystallinity, strain, and crystal defects. XRD peaks are produced by constructive interference of a monochromatic beam of X-rays scattered at specific angles from each set of lattice planes in a sample. The peak intensities are determined by the atomic positions within the lattice planes. Consequently, the XRD pattern is the fingerprint of periodic atomic arrangements in a given material. An online search of a standard database for X-ray powder diffraction pattern enables quick phase identification for a large variety of crystalline samples [54].

#### 3.3.1 (a) Principle of XRD

XRD is based on constructive interference of monochromatic X-rays and a crystalline sample. These X-rays are generated by a cathode ray tube, filtered to produce monochromatic radiation, collimated to concentrate and directed toward the sample. The interaction of the incident rays with the sample produces constructive interference (and a diffracted ray) when conditions satisfy Bragg's Law,

$$n\lambda = 2d \sin\theta \text{-------- (1)}$$

Where, n is an integer, $\lambda$ is the wavelength of the X-rays, d is the interplanar spacing generating the diffraction, and $\theta$ is the diffraction angle.

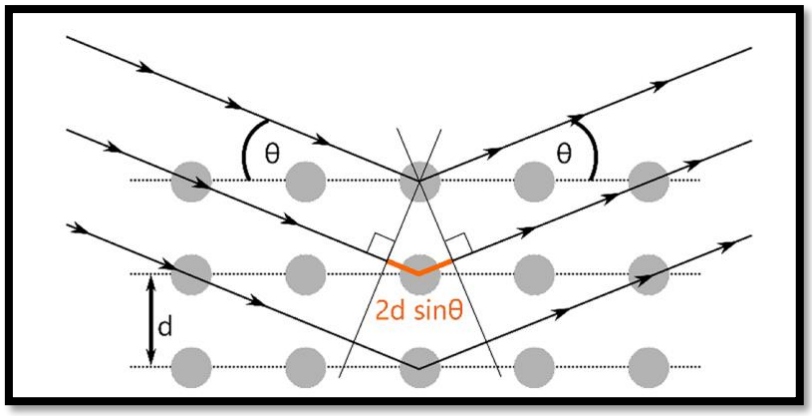


**Figure 3.1: Schematic diagram of Bragg's law**

This law relates the wavelength of electromagnetic radiation to the diffraction angle and the lattice spacing in a crystalline sample. These diffracted X-rays are then detected, processed and counted. By scanning the sample through a range of angles 2θ, all possible diffraction directions of the lattice should be attained due to the random orientation of the powdered material. Typically, this is achieved by comparison of d-spacings with standard reference patterns. All diffraction methods are based on generation of X-rays in an X-ray tube. These X-rays are directed at the sample, and the diffracted rays are collected. A key component of all diffraction is the angle between the incident and diffracted rays.

### 3.3.1 (b) Working and Instrumentation of XRD

An X-ray diffractometer consists of five major components: The X-ray source, the detector, the incident (or primary beam) optics, the receiving (or diffracted beam) optics, and the goniometer. The diffractometer is contained within a radiation enclosure and controlled by a computer.

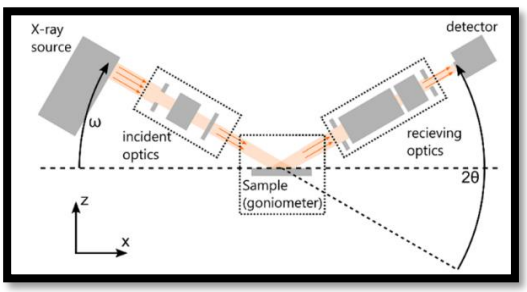


**Figure 3.2: Components of a diffractometer**


**Figure 3.3: Powder X-Ray Diffractometer instrument**

### 3.3.1 (c) Advantage of powder XRD

- It is relatively fast.
- Non-destructive.
- Very precise and if done correctly accurate.
- Probes a large proportion of the area of the film.
- Measurements under non-ambient conditions and in-situ measurements possible.

### 3.3.1 (d) Disadvantage of powder XRD

- The spatial resolution is poor.
- Some information can be hard to deconvolute, for example, compositional changes and strain in films will both lead to shifts in peak positions.

### 3.3.1 (e) Applications

X-ray powder diffraction is most widely used for the identification of unknown crystalline materials (e.g., minerals, inorganic compounds). Determination of unknown solids is critical to studies in geology, environmental science, material science, engineering and biology.Other applications include:

- Characterization of crystalline materials
- Identification of fine-grained minerals such as clays and mixed layer clays that are difficult to determine optically
- Determination of unit cell dimensions and measurement of sample purity

With specialized techniques, XRD can be used to:

- Determine crystal structures using Rietveld refinement
- Determine of modal amounts of minerals (quantitative analysis)
- Characterize thin films samples by:
    - Determining lattice mismatch between film and substrate and to inferring stress and strain
    - Determining dislocation density and quality of the film by rocking curve measurements
    - Measuring superlattices in multi-layered epitaxial structures
    - Determining the thickness, roughness and density of the film using glancing incidence X-ray reflectivity measurements
- Make textural measurements, such as the orientation of grains, in a polycrystalline sample [55,56].

### 3.3.2. FIELD EMISSION SCANNING ELECTRON MICROSCOPY (FESEM)

Field emission scanning electron microscopy (FE-SEM) is a type of microscope and advanced technology used to capture the microstructural image of the materials. FE-SEM is typically performed in a high vacuum because gas molecules tend to disturb the electron beam. The emitted secondary and backscattered electrons are used for imaging [57].

### 3.3.2 (a) Principle

FESEM is an electron microscope that uses a focused beam of electrons that react with the sample to produce a topological image and relative composition.

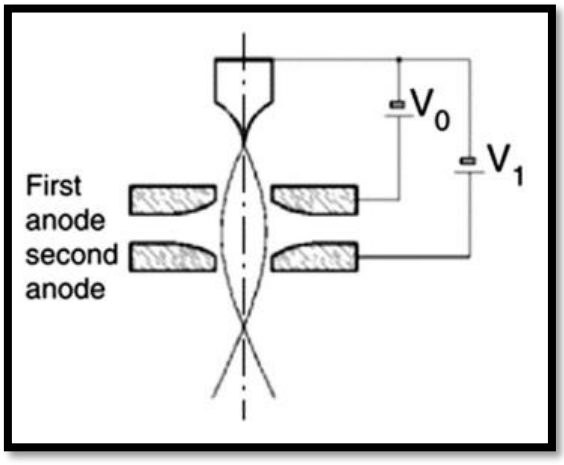


**Figure 3.4: Field Emission Gun working principles**

Upon contact with the sample, the focused beam of electron will produce secondary electrons (SEs), backscattered electrons, and characteristic X-ray, which is then detected with respective detectors and finally displayed on the monitor. The principles of operation involve two layers of anodes, which functions as an electrostatic lens to control the electron beams by extracting the electrons using the first anode and accelerates it using the second one.

### 3.3.2 (b) Instrumentation and Working

The electron gun consisting of cathode and anode. The condenser lens controls the number of electrons travelling down the column. The objective lens focuses the beam into a spot on the sample. Deflection coil helps to deflect the electron beam. The secondary electron detector (SED) attracts the secondary electrons. Among them, additional sensors detect backscattered electrons and X-rays. Electrons are liberated from a field emission source and accelerated in a high electrical field gradient. Within the high vacuum column these so-called primary electrons are focused and deflected by electronic lenses to produce a narrow scan beam that bombards the object.

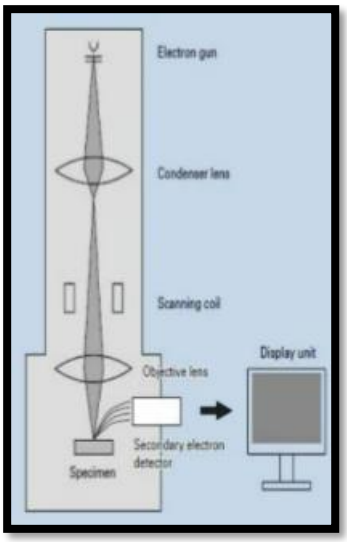


**Figure 3.5: Schematic representation of FESEM**

As a result, secondary electrons are emitted from each spot on the object. The angle and velocity of these secondary electrons relates to the surface structure of the object. A detector catches the secondary electrons and produces an electronic signal. This signal is amplified and transformed to a video scan-image that can be seen on a monitor or to a digital image that can be saved and processed further [58].

### 3.3.2 (c) Advantage of FESEM

- The ability to examine smaller-area contamination spots at electron accelerating voltages compatible with energy dispersive spectroscopy (EPS).
- Reduced penetration of low-kinetic-energy electrons probes closer to the immediate material surface.
- High-quality, Low-voltage images with negligible electrical charging of samples (accelerating voltages ranging from 0.5 to 30 kilovolts).
- Essentially no need for placing conducting coatings on insulating materials [59].

### 3.3.2 (d) Disadvantage of FESEM

- The main disadvantages are cost, size, maintenance, researcher training and image artifacts resulting from specimen preparation.
- This type of microscope is a large, cumbersome, expensive piece of equipment, extremely sensitive to vibration and external magnetic fields.

### 3.3.2 (e) Application of FESEM

- Semiconductor device cross section analyses for gate widths, gate oxides, film thicknesses and construction details.
- Advanced coating thickness and structure uniformity determination.
- Small contamination feature geometry and elemental composition measurement [60].

### 3.3.3 Thermogravimetric-Differential thermal analysis (TG-DTA)

Thermogravimetry is a technique measuring the variation in mass of a sample when it undergoes temperature scanning in a controlled atmosphere. This variation in mass can be either a loss of mass (vapour emission) or a gain of mass (gas fixation). Differential thermal analysis is a technique measuring the difference in temperature between a sample and a reference (a thermally inert material) as a function of the time or the temperature, when they undergo temperature scanning in a controlled atmosphere. The DTA method enables any transformation to be detected for all the categories of materials [61].

### 3.3.3 (a) Principle of TG-DTA

Thermogravimetry (TG) or Thermogravimetric Analysis (TGA), is an analytical technique in which a change in the weight of a substance is recorded as a function of temperature [62].

### 3.3.3 (b) Working Principles of TG-DTA

Thermal behaviour being one of the physical properties of any material, it gives fair estimation of constituents, nature and usage of material.

**Figure 3.6: Diagrammatic representation of TG-DTA**

The traditionally adopted procedures for thermogravimetry and calorimetry are tedious, time consuming and involve elaborate human intervention. Modern thermal analyzing systems overcome all the problems associated with the traditional techniques as they use versatile computers for setting up of experiment, its control, data acquisition/storage and analysis. Further, use of electronic sensors for physical measurements increases the sensitivity, accuracy and ease of operation [63].

### 3.3.3 (c) Advantages and Disadvantages of TG-DTA

- Temperature profile, atmosphere, sample are identical for both data sets - it eliminates uncertainty associated with differences in sample preparation, sampling, differing instruments and furnace materials, etc.

- Very often sacrifice on sample size happens (and consequently, sensitivity to small mass loss effects). Likewise (especially in TG-DTA systems) often sacrifice heat flow sensitivity (and thus the ability to observe small heat effects) also occurs [62].

### 3.3.3 (d) Applications of TG-DTA

- **Thermogravimetry (TG)**
    - Study thermal degradation
    - Chemical reaction resulting in changes of mass such as absorption, adsorption, desorption
    - Sample purity
- **Differential thermal analysis (DTA)**
    - Primarily used for detection of transition temperature
    - Sample purity

### 3.3.4 RAMAN SPECTROSCOPY

Raman spectroscopy is a technique used to observe vibrational, rotational, and other low-frequency modes. It has been commonly used in the field of material sciences and chemistry to provide the fingerprint to allow direct identification and interpretation of different molecules. this technique can be suitably applied for nondestructive, microscopic, chemical analysis, and imaging characterizations. when Raman spectroscopy is combined with electron microscopy, it can be used to offer better understanding of the complex mechanism involved in the inversion phase process as well as to determine the polymer chain structure in different areas across the membrane. Raman spectroscopy will help to understand the relationship between structure and transport properties, which could have an important impact on designing membranes for specific scientific problems.

### 3.3.4 (a) Principle

Raman scattering is the inelastic scattering of laser light impinged onto the sample and is scattered with a transfer of energy between the excitation light and the sample. Raman scattering occurs when the molecular motion produces a change in the polarizability of the molecule. The scattered light can be categorized as anti-Stokes or Stokes depending on their

energy level. The former has higher energy, whereas the latter has lower energy compared to the illumination light. When a molecule absorbs radiations, its energy increases in proportion to the photon. The increased energy may be at the level of the electronic, vibrational, or rotational energy of the molecule.

### 3.3.4 (b) Instrumentation

Either dispersive or non-dispersive spectrophotometers can be used. A prism or a grating is employed in the dispersive spectrophotometer, whereas, non-dispersive employs interferometer, analogous to Michelson interferometer in FTIR.

**Fundamental components of Raman spectrophotometer**

**1. Excitation source (Laser): -**Early Raman spectrometers employed mercury arc lamps, where a 435.8 nm line of coiled low-pressure mercury arc lamp was used as light source until 1960's. Laser sources became available in late 1960's and completely replaced the mercury lamp. There are a variety of lasers which can be used, e.g., Argon ion (488 and 514.5 nm), Krypton ion (530.9 and 647.1 nm), Helium–Neon (He–Ne) (632.8 nm), Near Infrared (IR) diode lasers (785 and 830 nm), Neodymium–Yttrium Aluminum Garnet (Nd: YAG) etc. Short wavelength sources, e.g., argon ion and krypton ion lasers generate considerable fluorescence and result in photodecomposition of the specimen. While, long wavelength sources, e.g., diode or (Nd: YAG) lasers can operate at very high power without decomposing the sample and also eliminate or reduce fluorescence.

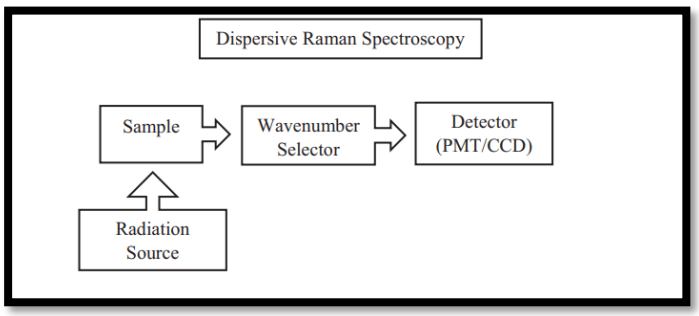


**Figure 3.7: a) Schematic for process involved in Raman spectra collection**

**2. Optics for sample illumination and light collection: -** Light from the irradiated/illuminated spot is collimated by a lens and guided to interference filter or spectrometer to get Raman spectrum.

**3. Wavelength selector (Filter or Spectrometer): -** Band pass filters are used to isolate a single laser beam. A combination of notch filter and high-quality grating monochromator is mostly employed in dispersive instruments. Double or even triple grating monochromators, super notch filters, rejection filters, holographic notch or edge filters and holographic filters are used to separate relatively weak Raman lines from intense Rayleigh scattered radiations.

**4. Detector (Photodiode array, CCD or PMT): -**Thermoelectrically cooled photomultiplier tubes and photodiode array detectors were used in early models of dispersive Raman spectrophotometers. Advances in instrumentation and technology replace these detectors with more sensitive charge transfer devices (CTDs) such as charge-coupled devices (CCDs) and charge-injection devices (CIDs). These devices act as a detector and used in the form of arrays. In CTD's arrays, photo-site converts the incoming optical signal into charge which is integrated and transferred to readout devices. Multichannel CCD detectors are used with laser wavelengths of less than 1 μm while single element low band-gap semiconductor such as Germanium (Ge) or Indium–Gallium–Arsenic (InGaAs) detectors are used with laser wavelengths of greater than 1 μm [64,65].

### 3.3.4 (c) Working

Unlike FTIR Spectroscopy that looks at changes in dipole moments, Raman looks at changes in a molecular bond's polarizability. Interaction of light with a molecule can induce a deformation of its electron cloud. This deformation is known as a change in polarizability. Molecular bonds have specific energy transitions in which a change of polarizability occurs, giving rise to Raman active modes. As an example, molecules that contain bonds between homonuclear atoms such as carbon-carbon, sulfur-sulfur, and nitrogen-nitrogen bonds undergo a change in polarizability when photons interact with them. These are examples of bonds that give rise to Raman active spectral bands, but would not be seen or difficult to see in FTIR.

Because Raman is an inherently weak effect, the optical components of a Raman Spectrometer must be well matched and optimized. Also, since organic molecules may have a greater tendency to fluoresce when shorter wavelength radiation is used, longer wavelength monochromatic excitation sources, such as solid-state laser diodes that produces light at 785 nm, are typically used [66].

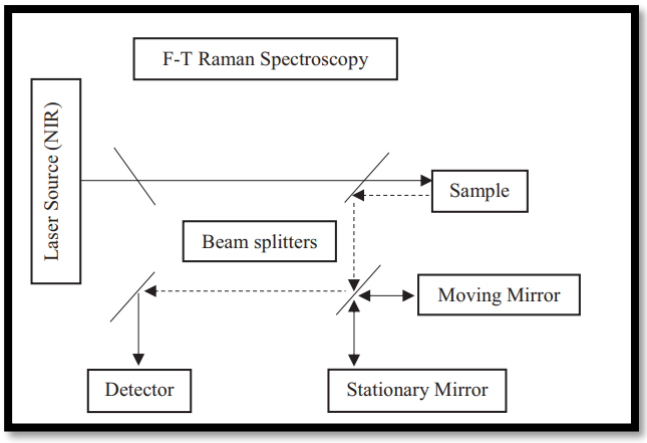


**Figure 3.7: b) Schematic for process involved in Raman spectra collection**

### 3.3.4 (d) Advantages

- Less sensitive to temperature changes.
- Minimally sensitive to water.
- Suitable on any surface since it measures scattered light, including opaque substrates.
- High specificity

### 3.3.4 (e) Disadvantages

- Prone to interference from other molecules when organic molecules are present.
- Unstable laser wavelength and intensity.
- Long collection time.
- Susceptible to noise interference (low signal to noise ratio), fluorescence and turbidity [67].

### 3.3.4 (f) Raman spectroscopy application

Raman spectroscopy is used in industry for a variety of applications, including:

- Crystallization Processes
- Polymorphism Identification
- Polymerization Reactions
- Hydrogenation Reactions
- Quality by Design

### 3.3.5 CYCLIC VOLTAMMETRY (CV)

**Cyclic voltammetry (CV)** is an electrochemical technique for measuring the current response of a redox active solution to a linearly cycled potential sweep between two or more set values. It is a useful method for quickly determining information about the thermodynamics of redox processes, the energy levels of the analyte and the kinetics of electronic-transfer reactions. CV is also invaluable to study electron transfer-initiated chemical reactions, which includes catalysis [68].

### 3.3.5 (a) Principle of CV

Cyclic voltammetry is a sophisticated potentiometric and voltammetric method. During a scan, the chemical either loses an electron (oxidation) or gains an electron (reduction) depending on the direction of the ramping potential. The magnitude of the current is proportional to the concentration of the analyte in solution, which allows cyclic voltammetry to be used in an analytical determination of concentration.

### 3.3.5 (b) Instrumentation

A CV system consists of an electrolysis cell, a potentiostat, a current-to-voltage converter, and a data acquisition system. The electrolysis cell consists of a working electrode, counter electrode, reference electrode, and electrolytic solution.

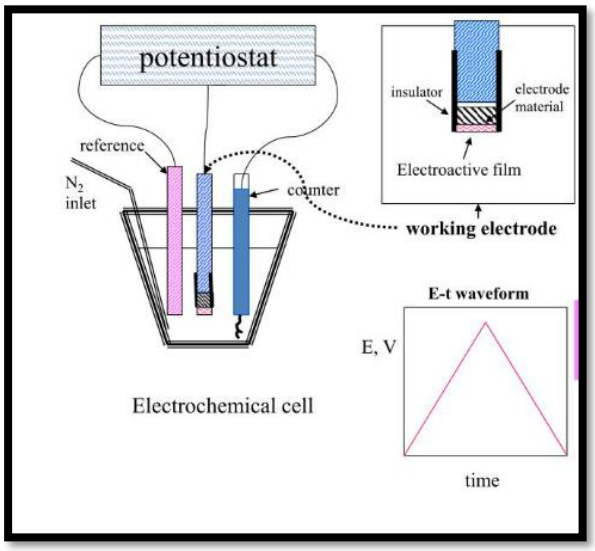


**Figure 3.8: Equipment for film voltammetry**

The working electrode's potential is varied linearly with time, while the reference electrode maintains a constant potential. The counter electrode conducts electricity from the signal source to the working electrode. The purpose of the electrolytic solution is to provide ions to the electrodes during oxidation and reduction. A potentiostat is an electronic device which uses a dc power source to produce a potential which can be maintained and accurately determined, while allowing small currents to be drawn into the system without changing the voltage. The current-to-voltage converter measures the resulting current, and the data acquisition system produces the resulting voltammogram [69].

**Electrodes**

The advent of modern electrochemistry created the need for electrodes and electrode setups. The most common arrangement today is the electrochemical cell with three different electrodes

- **Working electrode (WE)**
- **Reference electrode (RE)**
- **Counter electrode (CE)**

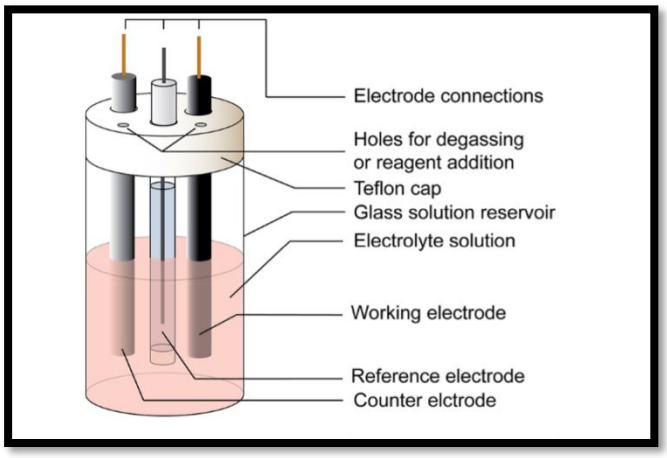


**Figure 3.9: Schematic representation of an electrochemical cell for CV experiments**

**Working Electrode (WE)**

The working electrode carries out the electrochemical event of interest. A potentiostat is used to control the applied potential of the working electrode as a function of the reference electrode potential. The most important aspect of the working electrode is that it is composed of redox inert material in the potential range of interest. When using electrodes such as glassy

carbon or platinum, clean electrodes surfaces can be prepared via mechanical polishing. To limit adsorption of solvent impurities, a treatment of the solvent with activated carbon can be used.

After recording a voltammogram, the WE is rinsed and then transferred to an electrolyte-only solution. If no electrochemical features are observed by CV, this rules out strong adsorption (although not weak adsorption). Since electrodes are capable of adsorbing species during an experiment, it is good practice to polish them after every experiment. Ideally, separate polishing pads are used before and after experiments to avoid contamination. Different electrode materials can also lead to varying electrochemical responses, such as when electron transfer kinetics differ substantially between electrode types, when adsorption occurs strongly on only certain electrode materials or when electrode specific reactivity with substrates occurs. As such, changing the electrode material is a good first step to diagnose and assess these issues.

**Reference Electrode (RE)**

A reference electrode has a well-defined and stable equilibrium potential. It is used as a reference point against which the potential of other electrodes can be measured in an electrochemical cell. There are a few commonly used (and usually commercially available) electrode assemblies that have an electrode potential independent of the electrolyte used in the cell. Some common reference electrodes used in aqueous media include,

- The saturated calomel electrode (SCE)
- Standard hydrogen electrode (SHE)
- AgCl/Ag electrode.

In nonaqueous solvents, reference electrodes based on the $Ag^+$ /Ag couple are commonly employed. These consist of a silver wire in a solution containing an $Ag^+$ salt, typically $AgNO_3$. The potential of $Ag^+$ /Ag reference electrodes can vary between experiments due to variations in $[Ag^+]$, electrolyte, or solvent used, so it is important to note the specific details of a nonaqueous reference electrode.

**Counter Electrode (CE)**

When a potential is applied to the working electrode such that reduction (or oxidation) of the analyte can occur, current begins to flow. The purpose of the counter electrode is to complete the electrical circuit. Current is recorded as electrons flow between the WE and CE. To ensure

the kinetics of the reaction occurring at the counter electrode does not inhibit those occurring at the working electrode, the surface area of the counter electrode is greater than the surface area of the working electrode. A platinum wire or disk is typically used as a counter electrode, though carbon-based counter electrodes are also available.

When studying a reduction at the WE, an oxidation occurs at the CE. As such, the CE should be chosen to be as inert as possible. Counter electrodes can generate byproducts depending on the experiment; therefore, these electrodes may sometimes be isolated from the rest of the system by a fritted compartment.

**Preparation of Electrolyte Solution**

As electron transfer occurs during a CV experiment, electrical neutrality is maintained via migration of ions in solution. As electrons transfer from the electrode to analyte, ions move in solution to compensate the charge and close the electrical circuit. A salt, called a supporting electrolyte, is dissolved in the solvent to help decrease the solution resistance. The mixture of the solvent and supporting electrolyte is commonly termed the "electrolyte solution".

**Solvent**

A good solvent has these characteristics: It is liquid at experimental temperatures. It dissolves the analyte and high concentrations of the supporting electrolyte completely. It is stable toward oxidation and reduction in the potential range of the experiment. It does not lead to deleterious reactions with the analyte or supporting electrolyte and it can be purified [70].

### 3.3.5 (c) Cyclic Voltammograms Explained

The 'duck-shaped' plot generated by cyclic voltammetry is called a cyclic voltammogram. In the example cyclic voltammogram shown, the scan starts at -0.4V and sweeps forward to more positive, oxidative potentials. Initially the potential is not sufficient to oxidise the analyte (a). As the potential approaches several kT of the standard potential, onset ($E_{onset}$) of oxidation is reached and the current exponentially increases (b) as the analyte is being oxidised at the working electrode surface. For a reversible process, here the current rises initially as if there is no change in the concentration of oxidant. The current is dictated by the rate of diffusion of oxidant to the electrode and the proportion converted to the reduced form according to the Nernst equation. The current response decreases from linearity as the analyte

is depleted and the diffuse double layer grows in size. The current reaches peak maximum at point (c) (anodic peak current ($i_{pa}$) for oxidation at the anodic peak potential ($E_{pa}$).

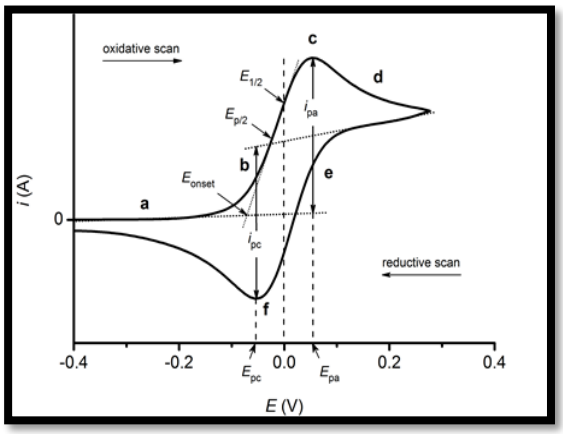


**Figure 3.10: 'Duck-shaped'- cyclic voltammogram**

The process is now under mixed control: more positive potentials cause an increase in current that is offset by a decreasing flux of analyte from further and further distance from the electrode surface.From this point the current is limited by the mass transport of analyte from the bulk to the Diffuse Double Layer (DDL) interface, which is slow on the electrochemical timescale and therefore does not satisfy the Nernst equation. This results in a decrease in current (d) as the potentials are scanned more positively until a steady-state is reached where further increases in potential no longer have an effect. Scan reversal to negative potentials (reductive scan) continues to oxidize the analyte until the applied potential reaches the value where the oxidized analyte which has accumulated at the electrode surface can be re-reduced (e). The process for reduction mirrors that for the oxidation, only with an opposite scan direction and a cathodic peak ($i_{pc}$) at the cathodic peak potential $E_{pc}$(f). The anodic and cathodic peak currents should be of equal magnitude but with opposite signs, provided that the process is reversible.

**Nernst Equation**

The Nernst equation relates the potential of an electrochemical cell (E) to the standard potential of a species ($E^{o}$) and the relative activities of the oxidized (Ox) and reduced (RED) analyte in the system at equilibrium. In the equation, F is Faraday's constant, R is the universal gas constant, n is the number of electrons, and T is the temperature

$$E = E^{o} + \frac{RT}{nF} \ln \frac{(Ox)}{(RED)} = E^{o} + 2.3026 \frac{RT}{nF} \log_{10} \frac{(Ox)}{(Red)} \qquad \text{--------} \ \textbf{(1)}$$

In application of the Nernst Equation to the one-electron reduction of Fc to Fc, the activities are replaced with their concentrations, which are more experimentally accessible, the standard potential E $^{o}$ is replaced with the formal potential E $^{o\prime}$, and n is set equal to 1.

$$E = E^{o'} + \frac{RT}{F}\ln\frac{[Fc+]}{[Fc]} = E^{o'} + 2.3026\frac{RT}{nF}\log_{10}\frac{[Fc+]}{[Fc]} \quad \text{----------} \ \textbf{(2)}$$

The Nernst equation provides a powerful way to predict how a system will respond to a change of concentration of species in solution or a change in the electrode potential

**Scan Rate**

The scan rate controls how fast the applied potential is scanned. Faster scan rates lead to a decrease in the size of the diffusion layer; as a consequence, higher currents are observed. For electrochemically reversible electron transfer processes involving freely diffusing redox species, the Randles- Sevick equation describes how the peak current $i_p$ (A) increases linearly with the square root of the scan rate υ (V $s^{-1}$), where n is the number of electrons transferred in the redox event, A ($cm^2$) is the electrode surface area, $D0$ ($cm^2$ $s^{-1}$) is the diffusion coefficient of the oxidized analyte, and $C^o$ ($molcm^{-3}$) is the bulk concentration of the analyte. N F$\nu D_o$

$$i_p = 0.446\ n\ FAC^{o}\left(\frac{nF\nu D0}{RT}\right)^{1/2} \quad \text{--------}\textbf{(3)}$$

The Randles-Sevick equation can give indications as to whether an analyte is freely diffusing in solution. As analyte can sometimes adsorb to the electrode surface, it is essential to assess whether an analyte remains homogeneous in solution prior to analyzing its reactivity. Randles-Sevcik equation can be used to calculate diffusion coefficients [71].

**3.3.5 (d) Advantage**

- Sensitivity -realistic detection limits for differential pulse polarography are around 50µg/L,
- Multi-component analysis-provided the half-wave potentials are at least 100mV apart.
- Equipment that is relatively simple and not particularly expensive for a computer-controlled device capable of polarography and voltammetry.
- A wide range of analytes -metallic ions, non-metallic ions and organic species can be detected.

### 3.3.5 (e) Disadvantage

- Relatively slow-due to purging time
- Matrix interference- due to complex formation, which can make a species not analyzable because the half-wave potential is outside the measurable range.

### 3.3.5 (f) Application of CV

- Cyclic Voltammetry can be used to study qualitative information about electrochemical processes under various conditions.

- Such as the presence of intermediates in oxidation-reduction reactions, the reversibility of a reaction.

- CV can also be used to determine the electron stoichiometry of a system, the diffusion coefficient of an analyte, and the formal reduction potential, which can be used as an identification tool.

- In addition, due to the dependence of concentration to current in a reversible, Nernstian system, concentration of an unknown solution can be determined by generating a calibration curve of current vs. concentration [72].

# CHAPTER 4

# RESULTS AND DISCUSSION

## 4.1 INTRODUCTION

This chapter deals with the characterization of the prepared pure $NaFePO_4$ and $NaFe_{0.98}La_{0.02}PO_4$ sample. The structural, vibrational, morphological and electrochemical behavior of the prepared sample is discussed in this chapter.

## 4.2 Thermal characterization

### 4.2.1 Thermogravimetric-Differential thermal analysis (TG-DTA)

Thermal analysis is carried out using the instrument TG/DTA-EXSTAR/6300 (Thermo Gravimetric Analyser). Figure 4.1 and 4.2 shows the thermogravimetric profiles of the precursor sample and this temperature dependent analysis is used to evaluate the possible reactions occurring at the time of synthesis of $NaFePO_4$ and is used to fix the calcination temperature for the preparation of expected product.

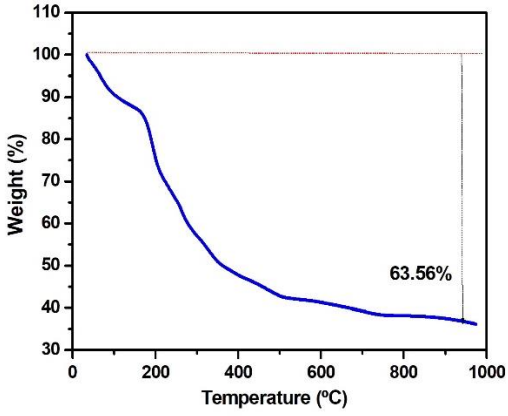


**Figure 4.1: Weight loss curve of precursor ($NaFePO_4$)**

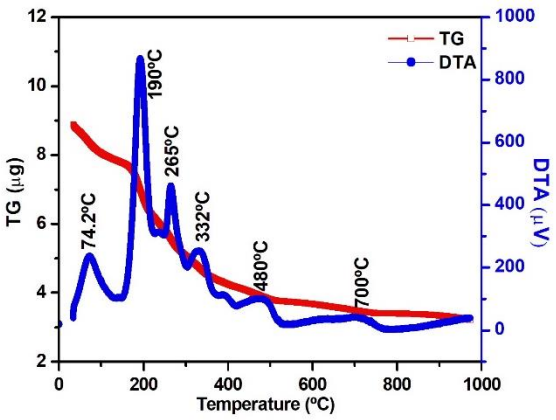


**Figure 4.2: TG-DTA of precursor ($NaFePO_4$)**

The analysis is carried out in temperature ranging from room temperature to 1000°C in nitrogen atmosphere. The TGA curves can be divided into five parts such as Room temperature (RT) - 100°C, 100°C - 173°C, 173°C - 265°C, 265°C - 339°C, 339°C - 483°C, 483°C - 746°C and 746°C - 1000°C regions. The first region shows 9.5% weight loss which is majorly from RT - 100°C corresponding to evaporation of moisture. The weight loss regions from 100 °C - 339 °C [73] corresponds to two processes of ferrous oxalate salt dehydration and decomposition. From the DTA curve, the peaks observed at 190 °C, 265°C and 332°C attributes

to the ferrous oxalate decomposition. The next weight loss 339 ºC -483ºC may be due to the decomposition of gelating agent i.e., citric acid. In other report, there is a prominent weight gain observed at 370 ºC and 495ºC which corresponds to the oxidation of iron from $Fe^{2+}$ to $Fe^{3+}$ [74] which is not observed in our case. Hence there is no change of state/oxidation of iron in the prepared sample. The temperature region from 480ºC - 700ºC shows a stable region of 8.14% residue after which the sample decomposes completely. From the DTA curve, an endothermic peak at 700ºC is observed and this temperature is chosen as the calcination temperature for the preparation of pure $NaFePO_4$ and the La-doped sample. The total weight loss of the precursor material is 63.56% as shown in Figure 4.1.

### 4.2.2 X-Ray Diffraction (XRD)

The crystal structure of the prepared samples are analysed by powder X-ray diffraction technique using the instrument PANAlytical XPert Pro. The X-Ray Diffraction **(**XRD) patterns of the pure $NaFePO_4$ and La-doped $NaFePO_4$ by sol-gel method are shown in Figure 4.3. All the diffraction peaks are indexed to ordered orthorhombic structure with a space group of Pnma.

From the XRD pattern of $NaFePO_4$ shows the major peaks are observed at 2θ = 20.85°, 24.20°, 33.24°, 34.31°, 35.75°, 41.00°, 49.50°, 54.16°, 57.68°, 62.62°, 64.12°, 72.15°, 75.66° with the hkl planes indexed to (101), (111), (121), (301), (002), (202), (222), (501), (141), (123), (313), (151), (423) respectively.

For $NaFe_{0.98}La_{0.02}PO_4$, the major peaks are observed at 2θ = 20.83°, 24.25°, 33.25°, 34.24°, 35.68°, 40.99°,49.52, 54.15°, 57.71°, 62.56°, 64.13°, 72.09°, 75.72° with the hkl planes indexed to (101), (111), (121), (301), (002), (222), (501), (141), (123), (313), (151), (423) respectively [75]. A small peak at 31° is observed for the doped sample whereas in the pure sample shows only a minor hump which may arise due to the effect of doping.

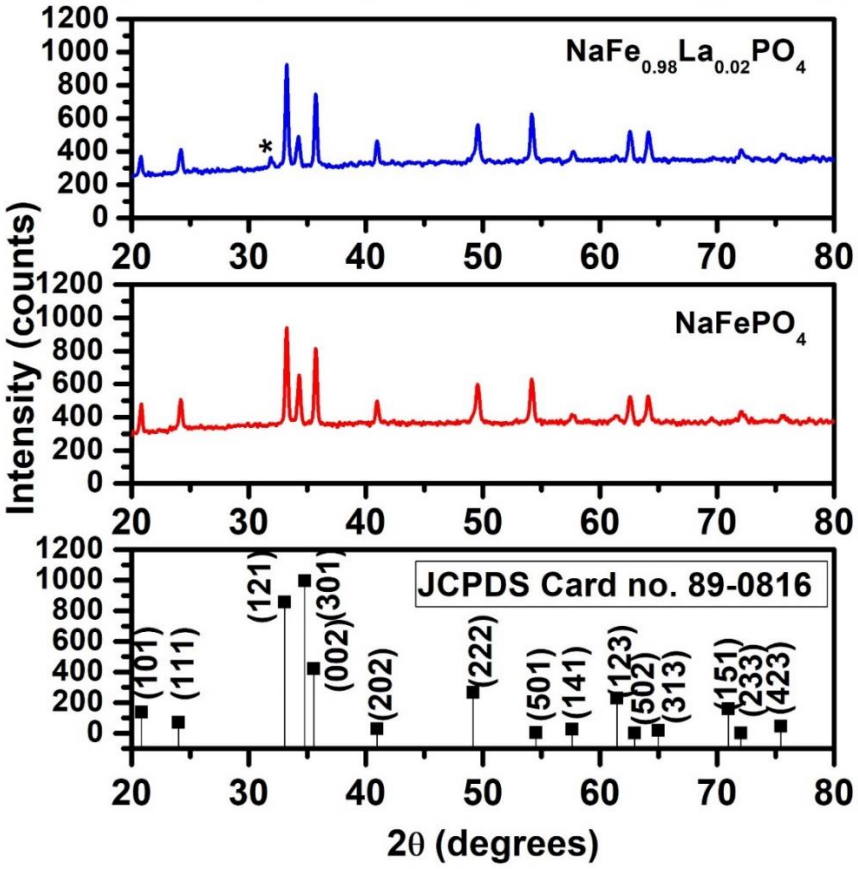


**Figure 4.3: XRD pattern of pure and La-doped $NaFePO_4$**

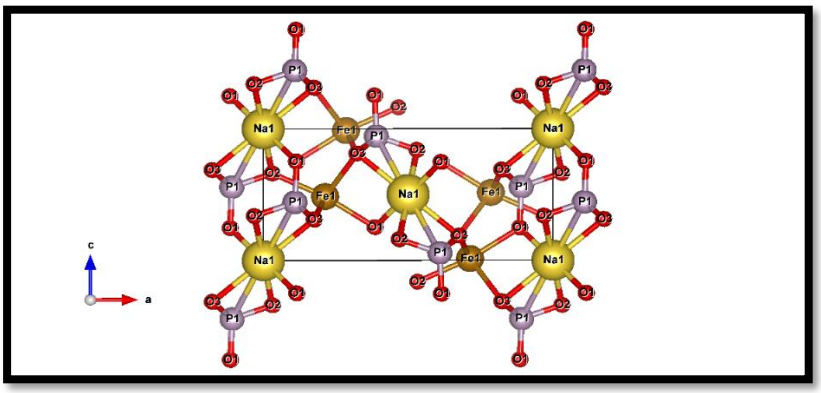


**Figure 4.4: Structure of $NaFePO_4$ drawn using the VESTA software**

The figure 4.4 indicates the crystal structure of $NaFePO_4$ drawn using the VESTA software. The atomic position of Na, Fe, P and O atoms are mentioned.

The intensity of the pure and the doped sample varies and higher intense peaks are observed for the La doped $NaFePO_4$. The lattice parameters of $NaFePO_4$ are a=8.017Å, b=6.791 Å and c=5.021 Å and a slight variation has been observed in lattice constants for the doped sample

a=8.031 Å, b=6.975 and c=5.029 Å. The ionic radii of the dopant $La^{3+}$ is 1.06 Å. Replacement of $La^{3+}$ in the place of Iron (Fe) is aimed during synthesis, and the ionic radii compatibility is ensured. Upon doping of La into the host matrix, there are no remarkable changes observed in the lattice parameters. The volume of the system is 273.45 $Å^3$ whereas the volume has been increased in La doped sample as 281.80 $Å^3$.

The crystallite size D, can be estimated from the peak width using Scherrer's formula. The Debye Scherrer formula is,

$$\mathbf{D=}\boldsymbol{k\lambda/\beta cos}\theta \textbf{ nm}$$

where,

λ is the X-ray wavelength (0.154 nm), β is the full width half maximum (FWHM) of a diffraction peak (radian), θ is the diffraction angle, k is the Scherrer's constant of the order of unity (0.9). The calculated values of FWHM, d-spacing, crystallite size and strain values are given in Table 4.1. The crystallite size of doped sample remains as similar to the pure $NaFePO_4$ indicating the occupation of La in the regular site and not in any of the interstitial position. The change is too low for an interstitial occupancy and corresponds only to the difference in ionic radii.

**Table 4.1: Crystallite sizes and lattice parameters of $NaFePO_4$ and $NaFe_{0.98}La_{0.02}PO_4$**

| **Samples** | **2θ (121) (deg)** | **β (FWHM) (deg)** | **$d_{(121)}$ (Å)** | **Crystallite size $D_{(121)}= K\lambda/\beta cos\theta$ nm** | **Strain ε** |
|---|---|---|---|---|---|
| $NaFePO_4$ | 33.24 | 0.2007 | 2.690 | 41.3 | 0.1732 |
| $NaFe_{0.98}La_{0.02}PO_4$ | 33.25 | 0.2007 | 2.694 | 41.31 | 0.1729 |

It is to be noted that the sharpness, interplanar spacing and crystallite size at (121) plane at 33.24° is very similar. Hence, it can be concluded that the occupation of Lanthanum should be in any of the regular site and not in the interstitial position.

**Table 4.2: Indexing planes of $NaFePO_4$**

| No. of. peaks | 2θ (deg) | h | k | l | $1/d^2$ |
|---|---|---|---|---|---|
| 1. | 33.24 | 1 | 2 | 1 | 0.0985 |
| 2. | 35.75 | 0 | 0 | 2 | 0.0793 |
| 3. | 34.31 | 3 | 0 | 1 | 0.0863 |
| 4. | 54.16 | 5 | 0 | 1 | 0.1174 |
| 5. | 49.50 | 2 | 2 | 2 | 0.1537 |
| 6. | 24.20 | 1 | 1 | 1 | 0.0768 |
| 7. | 20.85 | 1 | 0 | 1 | 0.0552 |
| 8. | 64.12 | 3 | 1 | 3 | 0.1873 |
| 9. | 62.62 | 1 | 2 | 3 | 0.1778 |
| 10. | 41.00 | 2 | 0 | 2 | 0.1104 |
| 11. | 72.15 | 1 | 5 | 1 | 0.1636 |
| 12. | 57.68 | 1 | 4 | 1 | 0.1419 |
| 13. | 75.66 | 4 | 2 | 3 | 0.2245 |

**Table 4.3: Indexing planes of $NaFe_{0.98}La_{0.02}PO_4$**

| No. of. Peaks | 2θ (deg) | h | k | l | $1/d^2$ |
|---|---|---|---|---|---|
| 1. | 33.25 | 1 | 2 | 1 | 0.0961 |

| | | | | | |
|---|---|---|---|---|---|
| 2. | 35.68 | 0 | 0 | 2 | 0.0790 |
| 3. | 54.15 | 5 | 0 | 1 | 0.1170 |
| 4. | 49.52 | 2 | 2 | 2 | 0.1511 |
| 5. | 62.56 | 1 | 2 | 3 | 0.1751 |
| 6. | 34.24 | 3 | 0 | 1 | 0.0860 |
| 7. | 64.13 | 3 | 1 | 3 | 0.1856 |
| 8. | 24.25 | 1 | 1 | 1 | 0.0755 |
| 9. | 40.99 | 2 | 0 | 2 | 0.1100 |
| 10. | 20.83 | 1 | 0 | 1 | 0.0550 |
| 11. | 57.71 | 1 | 4 | 1 | 0.1372 |
| 12. | 72.09 | 1 | 5 | 1 | 0.1577 |
| 13. | 75.72 | 4 | 2 | 3 | 0.2216 |

### 4.2.3 Raman analysis

The local structure of $NaFePO_4$ and $NaFe_{0.98}La_{0.02}PO_4$ are investigated by laser Raman spectroscopy. Fig 4.5 shows the Raman spectra of $NaFePO_4$, the peaks at 221, 291, 403, 606 and 1308 $cm^{-1}$ and Fig 4.6 shows the Raman spectra of $NaFe_{0.98}La_{0.02}PO_4$**,** the peaks at 229, 293, 406, 489, 611 and 1306 $cm^{-1}$ are noticed. The deformation of $PO_4^{3-}$ is seen as a Raman mode at 403 $cm^{-1}$ of $NaFePO_4$ and 406 $cm^{-1}$ in the doped sample $NaFe_{0.98}La_{0.02}PO_4$ (Fig 4.6). The Raman shift appeared in the range of 489 $cm^{-1}$ (Fig 4.5) of $NaFePO_4$ and 489 $cm^{-1}$ (Fig 4.6) of $NaFe_{0.98}La_{0.02}PO_4$ belonging to Fe-O vibrations. The intramolecular stretching mode of $PO_4^{3-}$ is observed at 606 $cm^{-1}$ of $NaFePO_4$ and 611$cm^{-1}$ in the doped sample. The distinct peak at 1308 $cm^{-1}$ and 1306 $cm^{-1}$ corresponds to P=O stretching vibration in both the samples.

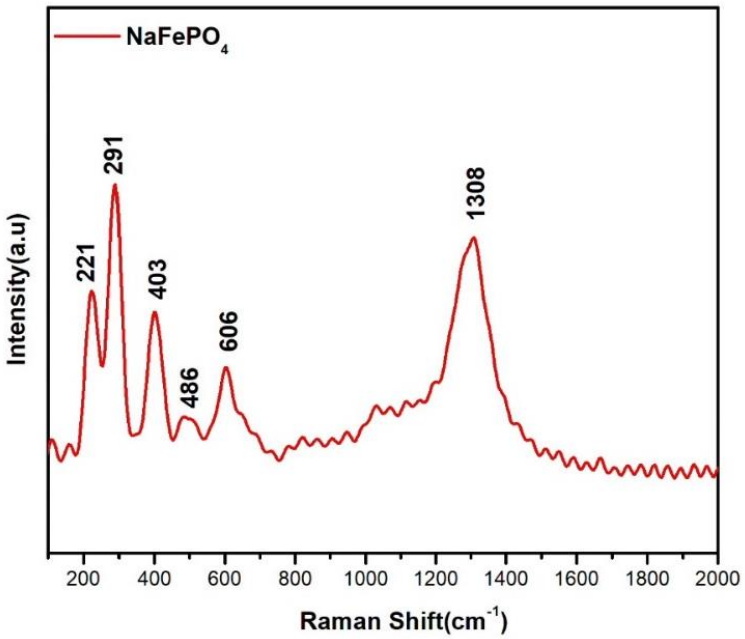


**Figure 4.5: Raman spectrum of $NaFePO_4$**

A higher wavenumber shift is observed for the doped sample. Usually, a shift in wavenumbers occurs due to the variation in chemical bond length of molecules. From the Raman analysis the doped sample $NaFe_{0.98}La_{0.02}PO_4$ is slightly altered due to the occupancy of La.

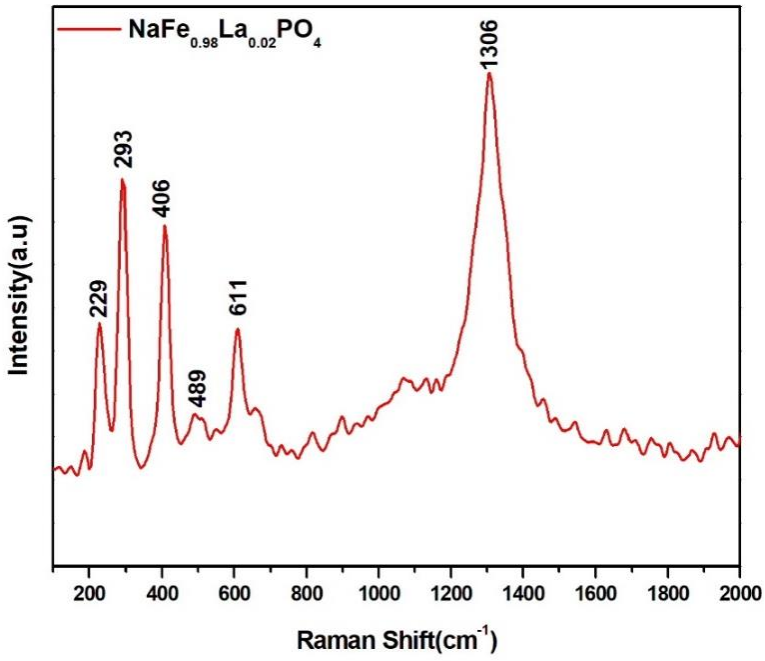


**Figure 4.6: Raman spectrum of $NaFe_{0.98}La_{0.02}PO_4$**

**Table 4.4: Assignments of Raman Peaks**

| S.No. | Raman shift($cm^{-1}$) for $NaFePO_4$ | Raman shift ($cm^{-1}$) for $NaFe_{0.98}La_{0.02}PO_4$ | Assignments | Ref. |
|---|---|---|---|---|
| 1. | 221 | 229 | Fe-O vibrations | Wang et al., (2019) [79] |
| 2. | 291 | 293 | | |
| 3. | 403 | 406 | Deformation of $PO_4^{3-}$ | Xudong et al., (2019) [76] |
| 4. | 489 | 489 | Fe-O vibrations | V. Priyanka.,et al(2017) [75] |
| 5. | 606 | 611 | Intramolecular stretching mode of $PO_4^{3-}$ | Fang et al., (2014) [77] |
| 6. | 1308 | 1306 | PO Stretching | Tibebe et. Al. (2019) [78] |

## 4.3 Morphological analysis

### 4.3.1 Field Emission Scanning Electron Microscopy (FESEM)

The Field Emission Scanning and transmission electron microscopy (FESEM) revealed plate like morphology. The La-doped sample shows cluster rod like particles.

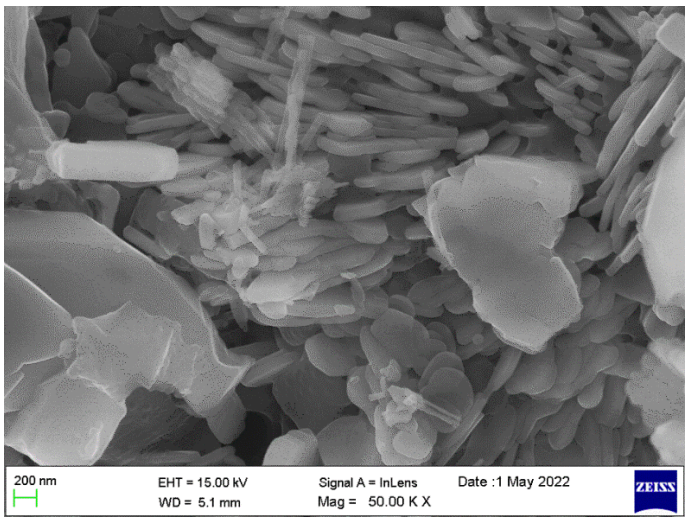


**Figure 4.7: FESEM image of $NaFePO_4$**

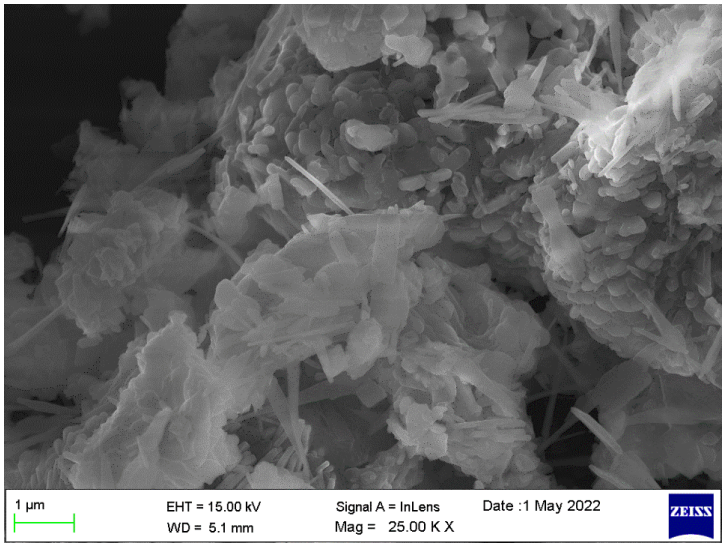


**Figure 4.8: FESEM image of $NaFe_{0.98}La_{0.02}PO_4$**

## 4.4 Cyclic Voltammetry (CV) analysis

The electrochemical performance of the $NaFePO_4$ and La doped $NaFePO_4$ is evaluated using Cyclic Voltammetry (CV). The conventional three electrode cell is used with $NaFePO_4$ and La doped $NaFePO_4$ as working electrode. A platinum and Ag/AgCl electrode were used as counter and reference electrodes respectively to study the electrochemical performance of the working electrode ($NaFePO_4$ and La doped $NaFePO_4$).

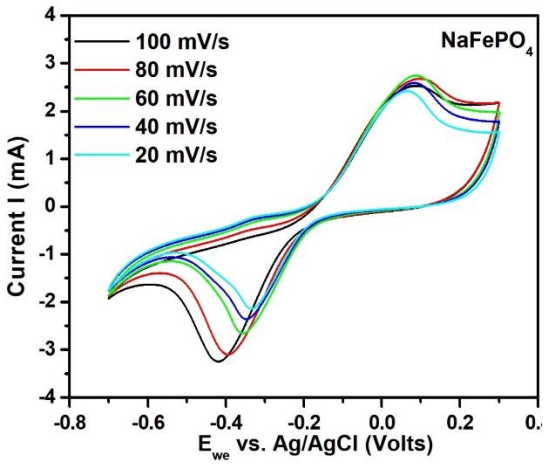


**Figure 4.9: CV curve of $NaFePO_4$**

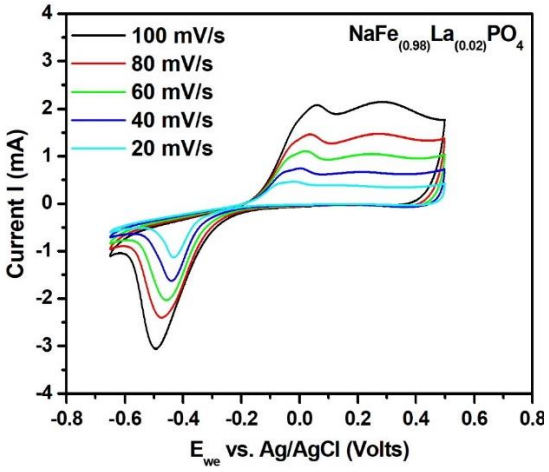


**Figure 4.10: CV curve of La-doped $NaFePO_4$**

Figure 4.9 shows the CV profile of $NaFePO_4$ with the electrolytic concentration of 1M-NaOH at different scan rates ranging from 20mV/s to 100mV/s. The peak current increases with scan rate which is in accordance with Randles-Sevcik equation.

$$i_p = 0.446\ n\ FAC^o\left(\frac{nF\nu D_o}{RT}\right)^{1/2}$$

where,

$i_p$ - Peak current (A),

n - The number of electrons transferred in the redox event,

A- Electrode surface area ($cm^2$),

Do - Diffusion coefficient ($cm^2s^2$),

$C^o$ - Bulk concentration (mol $cm^{-3}$).

As per this equation, when the scan rate increases, the peak current also increases as the diffusivity of the ions is constant. At the scan rate of 100 mV/s, a maximum current of 2.3 mA was obtained.

**Table 4.5: CV analysis of $NaFePO_4$ in 1M-NaOH electrolyte**

| **Scan rate (mV/s)** | **Potential (V)** | | **Current (mA)** | | | |
|---|---|---|---|---|---|---|
| | $E_{pa}$ | $E_{pc}$ | $I_{pa}$ | $I_{pc}$ | $\lvert E_{pc}-E_{pa}\rvert$ | $\lvert I_{pc}/I_{pa}\rvert$ |
| 100 | 0.079 | -0.419 | 1.893 | -2.094 | 0.498 | 1.8114 |
| 80 | 0.087 | -0.391 | 1.94 | -2.004 | 0.478 | 1.8152 |
| 60 | 0.082 | -0.358 | 1.916 | -1.674 | 0.44 | 1.7510 |
| 40 | 0.075 | -0.348 | 1.739 | -1.415 | 0.423 | 1.5757 |
| 20 | 0.059 | -0.335 | 1.563 | -1.325 | 0.394 | 1.6965 |

**Table 4.6: CV analysis of $NaFe_{0.98}La_{0.02}PO_4$ in 1M-NaOH electrolyte**

| Scan rate (mV/s) | Potential (V) | | Current (mA) | | $\|E_{pc}-E_{pa}\|$ | $\|I_{pc}/I_{pa}\|$ |
|---|---|---|---|---|---|---|
| | $E_{pa}$ | $E_{pc}$ | $I_{pa}$ | $I_{pc}$ | | |
| 100 | 0.05 | -0.492 | 1.7 | -2.42 | 0.542 | 1.423 |
| 80 | 0.03 | -0.474 | 1.19 | -1.92 | 0.504 | 1.613 |
| 60 | 0.007 | -0.459 | 0.87 | -1.62 | 0.466 | 1.862 |
| 40 | 0.003 | -0.442 | 0.56 | -1.29 | 0.445 | 2.303 |
| 20 | -0.01 | -0.43 | 0.29 | -0.77 | 0.42 | 2.655 |

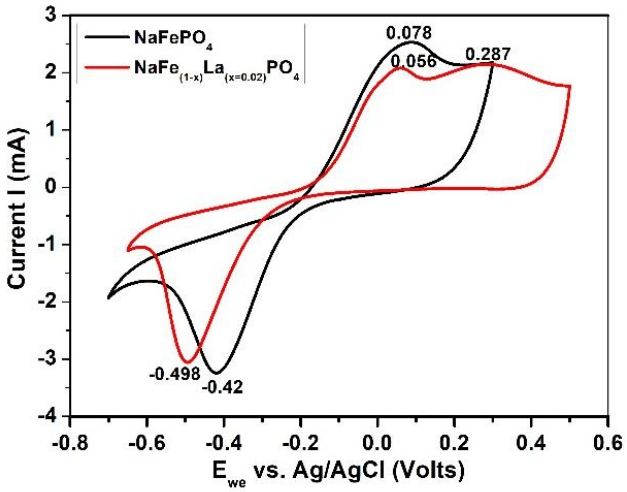


**Figure 4.11: Comparison of CV curve of pure and doped samples**

Figure 4.11 shows the comparison of CV profiles of $NaFePO_4$ and La-doped $NaFePO_4$ in 1M NaOH electrolyte at the scan rate of 100 mV/s. The potential window of the prepared $NaFePO_4$ lies between -0.7 to +0.3 V, whereas in the case of doped sample it is extended from -0.65 to +0.5V. The oxidation and reduction peaks of pure sample is 0.0789 and -0.4205V and for the doped sample there exists two oxidation peaks at 0.056V and 0.2872V and reduction potential at -0.498 respectively. The reduction potential of -0.420V of the pure sample shows the iron

reduction process. The potential observed at 0.056V for the doped sample may be due to the oxidation of phosphorus and the second oxidation peak may be due to the leaching of copper from the substrate. Since, the copper leaching occurs in the La doped sample, to reap the advantage of operative window in this case, it is recommended to use substrate other than copper.

The specific capacitance is calculated using the formula,

$$C_{sp} = \int_{E1}^{E2} i(E)dE/(E_2 - E_1)mv$$

Where, $\int_{E1}^{E2} i(E)dE$ is the integrated area of the instantaneous current over the range of cut off potentials $E_1$ and $E_2$, ($E_2$-$E_1$) is the working potential window of the electrochemical system, m is the mass of the working electrode in g and v is scan rate in mV/sec.

The specific capacitance value of pure $NaFePO_4$ is 14.3 $mAhg^{-1}$ and the La-doped sample exhibits a higher value of 26.5 $mAhg^{-1}$. Hence La-doped sample shows a higher value of specific capacitance than the pure sample. Although the electrochemical performance is enhanced in the doped sample, comparable to other reports (Table 4.7) the specific capacitance value remains low. This may be due to the effect of substrate and could be improved by the use of substrate other than copper.

**Table 4.7: Comparison of Specific capacitance of $NaFePO_4$**

| **Author [Year Of Publication]** | **Material Used** | **Method of Preparation** | **Electrochemical Performance** |
|---|---|---|---|
| **Hiratsuka et al., (2021) [74]** | Maricite $NaFePO_4$ | Melt quenching method | • Initial capacity of 115 $mAhg^{-1}$ at 1C.<br>• Excellent cycling stability of capacity retention of 91.3% of 800 cycles. |
| **Wang et al., (2019) [79]** | Maricite $NaFePO_4$ | Sol-gel method | • Specific capacity after five cycles is as high as 140 $mAhg^{-1}$ which is 91% |

| | | | |
|---|---|---|---|
| | | | of theoretical capacity of $NaFePO_4$. |
| **Zhuet al., (2018) [25]** | NFP/C composites | Ball milling method | • High capacity of 78 $mAhg^{-1}$ even at a very high rate of 50 C. |
| **Wu et al., (2016) [80]** | $Na_4Fe_3(PO_4)_2P_2O_7$ nanocomposite | Sol-gel method | • Initial discharge capacity of 110 $mAhg^{-1}$ at 0.05 C and 25° C. |
| **Kawabeet al., (2011) [81]** | Carbon-coated $Na_2FePO_4F$ | Solid state method | • Initial discharge capacity of 110 mAh $g^{-1}$ at a rate of 1/20 C (6.2 $mAg^{-1}$) with well-defined voltage plateaus at 3.06 and 2.91 V vs. Na metal. |
| **This work** | Pure $NaFePO_4$<br>$NaFe_{0.98}La_{0.02}PO_4$ | Sol-gel method | • Specific capacitance value of 14.3 $mAhg^{-1}$ for pure sample and 26.5 $mAhg^{-1}$ for La-doped sample. |

# CHAPTER V

## SUMMARY AND CONCLUSION

Sodium iron phosphate ($NaFePO_4$) and La doped $NaFePO_4$ ($NaFe_{0.98}La_{0.02}PO_4$) are successfully synthesized by sol-gel method. From TG/DTA analysis, there is no change of state/oxidation of iron in the prepared samples since no weight gain is observed. From the DTA curve, an endothermic peak at 700 $^oC$ is observed and it is chosen as the calcination temperature for the preparation of pure $NaFePO_4$ and La-doped $NaFePO_4$. The crystal structure of the prepared samples are analysed by powder X-ray diffraction technique and all the diffraction peaks are indexed to ordered orthorhombic structure with a space group of Pnma. The crystallite size of doped sample remains as similar to the pure $NaFePO_4$ indicating the occupation of La in the regular site and not in any of the interstitial positions. From the Raman spectroscopy, the peaks are analysed to various vibrational bonds and indicates a usual behaviour of phosphorus modes. A higher wavenumber shift is obtained for the doped sample which confirms the incorporation of dopants in the lattice caused due to the variation in chemical bond length on substitution of atoms. FESEM of $NaFePO_4$ revealed plate like morphology and La-doped sample showed cluster rod like particles. The prepared sample is tested for cyclability with 1M NaOH as electrolyte, Pt as counter electrode and Ag/AgCl as reference electrode in three-electrode configuration. From the CV analysis, the specific capacitance value of pure $NaFePO_4$ is 14.3$mAhg^{-1}$ and La-doped sample exhibits a higher value of 26.5 $mAhg^{-1}$. Upon doping, two oxidation peaks are observed for the doped sample, first oxidation peak observed at 0.056V may be due to the oxidation of phosphorus and second oxidation peak observed at 0.287V may be due to the leaching of copper from the substrate. Improved electrochemical performance is expected by using an appropriate substrate other than copper. The scope of this work is to vary the dopant concentration, to identify the suitable substrate and to assemble a two-electrode device and testing.

**References:**


1. **Jang-Yeon Hwang, Seung-Taek Myung and Yang-Kook Sun**, Sodium-ion batteries: present and future, Royal Society of Chemistry, Volume-46, Pages-3529 to 3614,2017

2. **Swagatika Kamila, Bikash Kumar Jena and Suddhasatwa Bas,** Advances in Electrochemical Energy Storage Device: Supercapacitor, Energy Storage, Pages-119 to 148,2021

3. **Johannes Lindorfer, Daniel Cenk Rosenfeld, Hans Böhm,** Fuel Cells: Energy Conversion Technology, Energy institute at the johannes kepler university linz, linz, Austria, Pages-495 to 517,2020

4**. F Decker, S Cattarin**, Photoelectrochemical cells, Encyclopedia of Electrochemical Power Sources, Pages-1 to 9,2009

5. **Marin S. Halper James C. Ellenbogen,** Supercapacitors: A Brief Overview, MITRE Nanosystems Group, March 2006.

6. **M. Stanley Whittingham**, History, Evolution, and Future Status of Energy Storage, Proceedings of the IEEE, Volume- 100, Pages-0018 to 9219, 2012.

7. https://byjus.com/chemistry/battery-types/

8.https://collegedunia.com/exams/types-of-battery-primary-and-secondary-cell-and-their-uses-physics-articleid-1434.

9. https://www.brookings.edu/blog/techtank/2015/09/15/five-emerging-battery-technologies-for-electric-vehicles/

10. **Eider Goikolea, Verónica Palomares, Shijian Wang, Idoia Ruiz de Larramendi, Xin Guo, Guoxiu Wang and Teofilo Rojo**, Na-Ion Batteries-Approaching Old and New Challenges, Advanced Energy Materials, Volume-10, Issue-44, 2020.

11. https://patents.google.com/patent/WO2017067994A1/en

12. Hongyan Kang, Yongchang Liu, Kangzhe Cao, Yan Zhao, Lifang Jiao, Yijing Wang and Huatang Yuan, Update on anode materials for Na-ion batteries, **Journal of Materials Chemistry A**, Volume-3, Pages-17899 to 17913,2015

13. **Archana Chandra, Angesh Chandra & R S Dhundhel,** Electrolytes for sodium ion batteries: A short review, Indian Journal of Pure & Applied Physics, Volume-58, Pages-113 to 119, 2020

14. **Yan yu**, Binders for Sodium-Ion Batteries, Wiley online library, Advanced functional materials, 18 February 2022.

15. **Christoph Vaalma, Daniel Buchholz, Marcel Weil and Stefano Passerini,** A cost and resource analysis of sodium-ion batteries, Vaalma, C., Buchholz, D., Weil, M. et al. A cost and resource analysis of sodium-ion batteries. Nature Reviews Materials, Volume-3**,** Article No-18013, 2018

16. www.sciencedirect.com/topics/engineering/sodium-ion-battery

17.**Yongjie Cao, Chen Yang, Yao Liu, Xiuping Xia, Deqiang Zhao, Yuanjie Cao, Haishen Yang, Junxi Zhang,Jing Lu and Yongyao Xia**, A New Polyanion $Na_3Fe_2(PO_4)P_2O_7$ Cathode with High Electrochemical Performance for Sodium-Ion Batteries, ACS Energy Letters, Volume-5, Issue-12, Pages-3657 to 3890, 2020

18.**Baskar Senthilkumar, Angalakurthi Rambabu, Chinnasamy Murugesan, Saluru Baba Krupanidhi, and Prabeer Barpanda**, Iron-Based Mixed Phosphate $Na_4Fe_3(PO_4)_2P_2O_7$ Thin Films for Sodium-Ion Microbatteries, ACS Publications, Volume-5, Pages-7219 to 7214, 2020.

19.**Carlos Berlanga, Iciar Monterrubio, Michel Armand, Teófilo Rojo, Montserrat Galceran, and Montse Casas-Cabanas**, Cost-effective synthesis of triphylite-$NaFePO_4$ cathode: a zero-waste process, ACS Sustainable Chemistry and Engineering, Pages-1 to 21,30 Dec 2019.

20.**Xiangjun Pu, Chao Rong, Shenglong Tang, Huiming Wang, Shunan Cao, Yan Ding, Yuliang Cao and Zhongxue Chen,** Zero-strain $Na_4Fe_7(PO_4)_6$ as a novel cathode material for sodium-ion batteries, Chemical Communications, Volume-55, Pages-9043 to 9046, 2019.

21.**Xiuping Xia, Yongjie Cao, Liu Yao, Haishen Yang, Junxi Zhang,** MCNT-Reinforced $Na_3Fe_2(PO_4)_3$ as Cathode Material for Sodium-Ion Batteries, Arabian Journal for Science and Engineering, Volume-45, Pages-143 to 151, 2019.

22.**Navaratnarajah Kuganathan and Alexander Chroneos**, Defect Chemistry and Na-Ion Diffusion in $Na_3Fe_2(PO_4)_3$ Cathode Material, Materials, Volume-12, Article No-1348, 2019.

23.**Yongjie Cao, Yao Liu, Deqiang Zhao, Junxi Zhang, Xiuping Xia, Tong Chen, Lai-chang Zhang, Peng Qin, Yongyao Xia**, K-doped $Na_3Fe_2(PO_4)_3$ cathode materials with high-stable structure for sodium-ion stored energy battery, Journal of Alloys and Compounds, Volume-784, Pages-939 to 946, 2019.

24.**Seonghun Jeong, Byung Hoon Kim, Yeong Don Park, Chang Yeon Lee, Junyoung Mun, Artur Tron**, Artificially coated $NaFePO_4$ for aqueous rechargeable sodium-ion batteries, Journal of Alloys and Compounds, Volume-784, Pages-720 to 726, 2019

25.**Xiaobo Zhu, Takashi Mochiku, Hiroki Fujii, Kaibin Tang, Yuxiang Hu, Zhenguo Huang, Bin Luo, Kiyoshi Ozawa, and Lianzhou Wang**, A new sodium iron phosphate as a stable high-rate cathode material for sodium ion batteries, Nano Research, Volume-11, Pages-6197 to 6205, 2018.

26.**Yongchang Liu, Ning Zhang, Fanfan Wang, Xiaobin Liu, Lifang Jiao, and Li-Zhen Fan**, Approaching the Downsizing Limit of Maricite $NaFePO_4$ toward High-Performance Cathode for Sodium-Ion Batteries, Advanced Functional Materials, Volume-28, Issue-30, Article No-1801917, 2018.

27.**Roman Kapaev & Andrey Chekannikov & Svetlana Novikova & Sergey Yaroslavtsev & Tatiana Kulova & Vyacheslav Rusakov & Alexander Skundin & Andrey Yaroslavtsev**, Mechanochemical treatment of maricite-type $NaFePO_4$ for achieving high electrochemical performance, Journal Solid State Electrochemistry, Volume-21, Pages-2373 to 2380, 2017.

28.**Ghulam Ali, Ji-Hoon Lee, Dieky Susanto, Seong-won Choi, Byung Won Cho, Kyung-Wan Nam, and Kyung Yoon Chung**, Polythiophene-wrapped Olivine $NaFePO_4$ as a Cathode for Na-ion Batteries, ACS Applied Materials & Interfaces, Volume-8, Article No-15422, 2016.

29.**Wei Tang, Xiaohe Song,Yonghua Du, Chengxin Peng, Ming Lin, Shibo Xi, Bingbing Tian, Jiaxin Zheng, Yuping Wu, Feng Pan and Kian Ping Loh,** High-performance

$NaFePO_4$ formed by aqueous ion-exchange and its mechanism for advanced sodium ion batteries, Journal of Materials Chemistry A, Volume-4, Article No-4882, 2016

30.**Markas Law, Vishwanathan Ramar and Palani Balaya**, Synthesis, Characterisation and Enhanced Electrochemical Performance of Nanostructured $Na_2FePO_4F$ for Sodium Batteries, Royal Society of Chemistry Advances, Volume-5. Pages-50155 to 50164, 2015.

31.**Chun Li, Xue Miao, Wei Chu, Ping Wu and Dong Ge Tong,** Hollow amorphous $NaFePO_4$ nanospheres as a high-capacity and high-rate cathode for sodium-ion batteries, Journal of Materials Chemsitry A, Volume-6, Article No- 13979, 2018.

32.**N.V. Kosova, V.R. Podugolnikov, E.T. Devyatkina, A.B. Slobodyuk**, Structure and electrochemistry of $NaFePO_4$ and $Na_2FePO_4F$ cathode materials prepared via mechanochemical route, Materials Research Bulletin, Volume- 60, Pages-849 to 857, 2014.

33.**Hamdi Ben Yahia, Daisuke Mori, Masahiro Shikano, Hironori Kobayashia and Yoshiyuki Inaguma,** Structural, magnetic, and electrochemical properties of the high-pressure form of $Na_2Co[PO_4]F$, Dalton Trans., Volume-43, Pages-13630 to 13636, 2014

34.**Yujie Zhu, Yunhua Xu, Yihang Liu, Chao Luo and Chunsheng Wang**, Comparison of electrochemical performances of olivine $NaFePO_4$ in sodium-ion batteries and olivine $LiFePO_4$ in lithium-ion batteries, Nanoscale, Volume-5, Article No-780, 2013.

35.**Alex Langrock, Yunhua Xu, Yihang Liu, Sheryl Ehrman, Ayyakkannu Manivannan, Chunsheng Wang,** Carbon coated hollow $Na_2FePO_4F$ spheres for Na-ion battery cathodes, Journal of Power Sources, Volume-223, Pages-62 to 67, 2013

36.**Prabeer Barpanda, Tian Ye, Shin-ichi Nishimura, Sai-Cheong Chung, Yuki Yamada, Masashi Okubo, Haoshen Zhou, Atsuo Yamada**, Sodium iron pyrophosphate: A novel 3.0 V iron-based cathode for sodium-ion batteries, Electrochemistry Communications, Volume-24, Pages-116 to 119, 2012

37.**Ann Sun, Faith R. Beck, Daniel Haynes, James A. Poston Jr, S.R. Narayanan, Prashant N. Kumta, A. Manivannan**, Synthesis, characterization, and electrochemical studies of chemically synthesized $NaFePO_4$, Materials Science and Engineering B, Volume-177, Pages-1729 to 1733, 2012.

38. **Seung-Min Oh, Seung-Taek Myung, Jusef Hassoun, Bruno Scrosati, Yang-Kook Sun,** Reversible $NaFePO_4$ electrode for sodium secondary batteries, Electrochemistry Communications, Volume-22, Pages-149 to 152, 2012

39.**Yoshiteru Kawabe, Naoaki Yabuuchi, Masataka Kajiyama, Norihito Fukuhara, Tokuo Inamasu, Ryoichi Okuyama, Izumi Nakai, Shinichi Komaba**, Synthesis and electrode performance of carbon coated $Na_2FePO_4F$ for rechargeable Na batteries, Electrochemistry Communications, Volume-13, Pages-1225 to 1228, 2011

40.**Trad K., Carlier D., Wattiaux A., Ben Amara M., Delmas C**, Study of a layered iron (III) phosphate phase $Na_3Fe_3(PO_4)_4$ used as positive electrode in lithium batteries, Journal of the Electrochemical Society, Volume-157, Issue-8, Pages-A947 to A952, 2010

41.**Fitria Rahmawati, Dwi Aman Nur Romadhona, Desi Dyah Paramita, Witri Wahyu Lestari**, Preparation of a $NaFePO_4$ Cathode Material via Electrochemical Sodiation of $FePO_4$ Layers on Al Substrates, International Journal of Technology, Volume-13, Pages-168 to 178, 2022.

42.**Jia Hui Bong and Stefan Adams**, Molecular dynamics simulations of amorphous NaFePO4 as an Na-ion battery cathode material, Functional Materials Letters, Volume-14, Article No-2141006, 2021.

43.**Fitria Rahmawati, Dwi Aman Nur Romadhona, Syulfi Faiz**, $NaFePO_4$ Cathode Prepared from The Caustic Fusion of A Mix Ilmenite-hematite Sand Followed by Cyclic Voltammetry for Na Insertion, J. Pure App. Chem. Res., Volume-9, Pages-142 to 152, 2020.

44.**Matthias Hildera, Patrick C. Howletta, Damien Saurel, Henri Anneb, Montse Casas-Cabanasb, Michel Armand, Teofilo Rojo, Douglas R. MacFarlane, Maria Forsytha**, Stable cycling of $NaFePO_4$ cathodes in high salt concentration ionic liquid electrolytes,Journal of power sources, Volume-406, Pages-70 to 80, 2018.

45.**Xiaobin Chen, Ke Du, Yanqing Lai, Guozhi Shang, Huangxu Li, Zhiwei Xiao, Yuxiang Chen, Junming Li, Zhian Zhang**, In-situ carbon-coated $Na_2FeP_2O_7$ anchored in three-dimensional reduced graphene oxide framework as a durable and high-rate sodium-ion battery cathode, Journal of power sources, Volume-357, Pages-164 to 172, 2017.

46.**Ling Zhao, Dengmei Zhou, Wanxia Huang, Xueya Kang, Qiwu Shi, Zhilin Deng, Xianwei Yan, Yongbo Yu**, Electrochemical Performances of Maricite $NaFePO_4$/C as cathode

material for Sodium-Ion and Lithium-Ion Batteries, Int. J. Electrochem. Sci., Volume-12, Pages- 3153 to 3165, 2017.

47.**Wenjiao Yao, Moulay-Tahar Sougrati, Khang Hoang, Jianing Hui, Philip Lightfoot, and Anthony Robert Armstrong**, $Na_2$ Fe ($C_2$ O $_4$) $F_2$: A New Iron-Based Polyoxyanion Cathode for Li/Na Ion Batteries, *Chemistry of Materials*, Volume-29, Pages-2167 to 2172, 2017.

48.**Su-Bin Yang and Jong-tae Son**, Synthesis and characterization of carbon-coated nano-sized $Na_{0.9}FePO_4$, Journal of the Korean Physical Society, Volume-69, Pages-443 to 447, 2016.

49.**Jongsoon Kim, Dong-Hwa Seo, Hyungsub Kim, Inchul Park, Jung-Keun Yoo, Sung-Kyun Jung, Young-Uk Park, William A. Goddard III and Kisuk Kang**, Unexpected discovery of low-cost maricite $NaFePO_4$ as a high-performance electrode for Na-ion batteries, **Energy Environ. Sci.,** Volume-**8,** Pages-540 to 545, 2015

50.**Nithinai Wongittharom, Tai-Chou Lee, Chueh-Han Wang, Yi-Chen Wang and Jeng-Kuei Chang**, Electrochemical performance of Na/$NaFePO_4$ sodium-ion batteries with ionic liquid electrolytes, J. Mater. Chem. A, Volume-2, Article No-5655, 2014.

51.**Kuniko Chihara, Ayuko Kitajou, Irina D. Gocheva, Shigeto Okada, Jun-ichi Yamaki,** Cathode properties of $Na_3M_2(PO_4)_2F_3$ [M =Ti, Fe, V] for sodium-ion batteries, Journal of Power Sources, Volume-227, Pages-80 to 85, 2013.

52.**Yujie Zhu, Yunhua Xu, Yihang Liu, Chao Luo and Chunsheng Wang**, Comparison of electrochemical performances of olivine $NaFePO_4$ in sodium-ion batteries and olivine $LiFePO_4$ in lithium-ion batteries, Nanoscale, Volume-5, Article No-780, 2013

53.**K. Zaghiba, J. Trottier, P. Hovingtona, F. Brochua, A. Guerfia, A. Mauger b, C.M. Julien,** Characterization of Na-based phosphate as electrode materials for electrochemical cells, Journal of Power Sources, Volume-196, Pages-9612 to 9617, 2011

54.**Rajiv Kohli and K.L.Mittal,** Developments in Surface Contamination and Cleaning, Volume 12,Methods for Assessment and Verification of Cleanliness of Surfaces and Characterization of Surface Contaminants, Volume-12, Pages-23 to105,2019.

55. https://serc.carleton.edu/research_education/geochemsheets/techniques/XRD.html

56.**George F. Harrington, Jose Santiso**, Back-to-Basics tutorial: X-ray diffraction of thin films, Journal of Electroceramics, October 2021

57.**Ramadhansyah Putra Jaya,** Porous concrete pavement containing nanosilica from black rice husk ash, Department of Civil Engineering, College of Engineering, University of Malaysia Pahang, Kuantan, Malaysia,2020

58. https://www.vcbio.science.ru.nl/public/pdf/fesem_info_eng.pdf

59.https://photometrics.net/field-emission-scanning-electron-microscopy-fesem/

60.https://findanyanswer.com/what-is-difference-between-fesem-and-sem

61. http://www.chem.latech.edu/~upali/chem466/TA/TA.pdf

62.https://prgc.ac.in/uploads/study_material/Thermogravimetry_Principle%20and%20Theory.pdf267.pdf

63. https://www.bose.res.in/facilities/Technical_Cell/tg_dta.html

64.https://www.researchgate.net/post/What_are_the_advantages_and_disadvantages_in_using_an_STA_compared_to_standalone_DSC_and_

65. **P.S. Goh, A.F. Ismail, B.C. Ng,** Raman Spectroscopy, Universiti Teknologi Malaysia, Johor Bahru, Johor, Malaysia,2017

66.https://epgp.inflibnet.ac.in/epgpdata/uploads/epgp_content/S000831ME/P001676/M030245/ET/1525950441Module-3_Unit5_COM-I.pdf

67.https://www.mt.com/in/en/home/applications/L1_AutoChem_Applications/Raman-Spectroscopy.html

68. **Wilbert Villena Gonzales, Ahmed Toaha Mobashsher and Amin Abbosh**, The progress of glucose- monitoring-A review of invasive to minimally and non-invasive techniques, Devices and sensors, Sensor, Volume-19, 800, 2019

69. https://www.ossila.com/pages/cyclic-voltammetry

70.https://chem.libretexts.org/Bookshelves/Analytical_Chemistry/Supplemental_Modules_(Analytical_Chemistry)/Instrumental_Analysis/Cyclic_Voltammetry

71. https://www.pineresearch.com/echem/files/LMECSPEXPT.pdf

72. **Noemie Elgrishi,´ Kelley J. Rountree, Brian D. McCarthy, Eric S. Rountree, Thomas T. Eisenhart, and Jillian L. Dempsey**, A Practical Beginner's Guide to Cyclic Voltammetry, J. Chem. Educ., Volume-95, Pages-197 to 206, 2018.

73.**Pavla Hermankova, Martin Hermanek, and Radek Zboril,** Thermal Decomposition of Ferric Oxalate Tetrahydrate in Oxidative and Inert Atmospheres: The Role of Ferrous Oxalate as an Intermediate**,** Eur. J. Inorg. Chem., Pages-1110 to1118, 2010.

74.**Masafumi Hiratsuka, Tsuyoshi Honma, Takayuki Komatsu**, Vitrification of maricite $NaFePO_4$ crystal by laser irradiation and enhanced sodium ion battery performance, Journal of Alloys and Compounds, Volume- 885, Article No-160928., 2021.

75**.V. Priyanka, R. Subadevi, M.Sivakumar**, Synthesis and structural analysis of $NaFePO_4$ nanocomposite for sodium ion batteries, International Research Journal of Engineering and Technology (IRJET) e-ISSN: 2395-0056 Volume- 04, Special Issue: 09, Sep -2017.

76. **Xudong Ma, Jiuyang Xia, Xuehang Wu, Zhiyi Pan, Pei Kang Shen,** Remarkable enhancement in the electrochemical activity of maricite $NaFePO_4$ on high-surface-area carbon cloth for sodium-ion batteries, carbon, Volume-146, Pages-78 to 87, 2019.

77. **Yongjin Fang, Lifen Qian, Xinping Ai, Hanxi Yang, Yuliang Cao**- Mesoporous Amorphous $FePO_4$ Nanospheres as High-Performance Cathode Material for Sodium-Ion Batteries, Nano Lett, Volume-14, Pages-339 to 3543, 2014.

78. **Dessie Tibebe, YezbieKassa and Ashok N. Bhaskarwar**, Treatment and characterization of phosphorus from synthetic waste water using aluminum plate electrodes in the electro coagulation process, BMC Chemistry, Volume-13, 2019.

79.**Duan Wanga, Yuanbo Wu, Jinmeng Lv, Rongrong Wang, Sailong Xu**, Carbon encapsulated maricite $NaFePO_4$ nanoparticles as cathode material for sodium-ion batteries, Colloids and Surfaces A, Volume-583, Article No-123957, 2019.

80.**Xuehang Wu, Guiming Zhong, Yong Yang**, Sol-gel synthesis of $Na_4Fe_3(PO_4)_2P_2O_7$ /C nanocomposite for sodium ion batteries and new insights into microstructural evolution during sodium extraction, Journal of Power Sources, Volume- 327, Pages-666 to 674, 2016

81.**Yoshiteru Kawabe, Naoaki Yabuuchi, Masataka Kajiyama, Norihito Fukuhara, Tokuo Inamasu, Ryoichi Okuyama, Izumi Nakai, Shinichi Komaba**, Synthesis and electrode performance of carbon coated $Na_2FePO_4F$ for rechargeable Na batteries, Electrochemistry Communications, Volume-13, Pages-1225 to 1228, 2011